nature communications

Article

https://doi.org/10.1038/s41467-025-67669-6

Computational design of allulose-responsive biosensor toolbox for auto-inducible protein expression and CRISPRi mediated dynamic metabolic regulation

Received: 21 April 2025

Accepted: 4 December 2025

Published online: 22 December 2025

Check for updates

Qianzhen Dong[1,2,3], Peng Chen[1,2], Zhiru Guo[1,3], Hongli Wei[1], Yan Zeng[1], Jingyu Zhang[1], Yan Men[1], Weidong Liu[1], Yuanxia Sun[1,2] ✉ & Jiangang Yang[1,2] ✉

Biosensors based on transcription factors (TFs) have shown extensive applications in synthetic biology. Due to the complex multi-domain structure of effector-TF-DNA, computational design of TFs remains a challenge. Here, we present the successful structure-guided computational design of the access tunnel, ligand binding, allosteric transition process for an allulose-responsive PsiR. It enables a 20-fold increase in sensitivity, reducing the EC_{50} of PsiR-allulose biosensors (PABs) from 16 mM to 0.8 mM, and delivers a PAB box possessing the detection range from 10 μM to 100 mM. We further validate its broader applicability in enhancing sensitivity of LacI-IPTG biosensor. Based on the developed PABs, we present the inducer-free allulose-mediated auto-inducible protein expression system, and demonstrate an allulose-triggered CRISPR interference circuit for dynamic metabolic regulation. It facilitates a 68% increase in allulose titer and achieves a high yield of 0.43 g/g glucose. This work provides the versatile TF toolbox for developing allulose-triggered regulation circuits in biotechnology application.

Transcription factors (TFs) represent a large class of regulators in cells to sense and adapt the changes of environmental and intracellular conditions[1]. The transcription-factor-based biosensors (TFBs) have shown great promise in biomanufacturing applications, including high-throughput screening[2], microbial strain engineering[3], metabolic dynamic control[4], protein engineering[5], and plug-and-play small molecule detection[6]. Although substantial advances have been made in discovering natural TFs with the aid of gene sequencing and bioinformatics, the TFBs based on wild-type TFs often suffer from limited output and unsuitable detection ranges[7]. These limitations arise from two main issues: i) the natural elements, such as promoters and RBSs, are often incompatible with non-native hosts; and ii) TFs themselves frequently lack the desired dynamic range, sensitivity, and specificity. To address these issues, strategies such as promoter and RBS optimization, as well as adjustment of plasmid copy number, have been employed to enhance TF expression in non-native systems[8–10]. In addition, directed evolution and site-directed mutagenesis have been used to alter effector specificity[11–13]; however, screening large mutational libraries is time-consuming and labor-intensive. Mechanistically, TF proteins perform the response process through three steps: i) effector access and binding to effector-binding domain (EBD); ii) allosteric transition from EBD to DNA-binding domain (DBD), and iii) conformational changes in the DBD that lead to dissociation from the DNA[14]. Due to the complex multi-domain structure of the effector-TF-DNA and unclear activation-allostery mechanisms, engineered TFs often suffer from high rates of inactivation (Is phenotype)[15–17].

[1]Tianjin Institute of Industrial Biotechnology, Chinese Academy of Sciences, Tianjin, China. [2]Key Laboratory of Engineering Biology for Low-carbon Manufacturing, Tianjin, China. [3]University of Chinese Academy of Sciences, Beijing, China. ✉e-mail: sun_yx@tib.cas.cn; yang_jg1@tib.cas.cn

To address these problems, computational design and engineering of TFs offers a promising yet challenging strategy.

Efficient and scalable protein expression systems are indispensable for manufacturing industrial enzymes and protein drugs[18–20]. Among these, the TF-based inducible expression systems offered a powerful solution. A preferred inducible system should have several key advantages: i) high sensitivity and broad dynamic range; ii) use of inducers that are inexpensive, stable, non-toxic, and minimal interference with cell metabolism; iii) ease of construction and applicability across diverse microbial hosts. To date, the LacI-IPTG system is the most widely used inducible platform in bacteria[21–23]. However, high cost, cell toxicity, and instability of inducer IPTG impeded its practical application in large-scale fermentation[24,25]. Other inducible expression systems based on AraC-arabinose[26], XylR-xylose[27], or MalR-maltose[28] have also been developed, yet they still face challenges such as inducer metabolic consumption, media component interference, and glucose-induced carbon catabolite repression. Recently, PsiR, a TF from *Agrobacterium tumefaciens* that responds to D-allulose, has attracted attention[29]. Notably, the inducer D-allulose, recognized as a safe sugar in food and dietary supplements, could not be metabolized by several model strains, including *Escherichia coli*, *Bacillus subtilis*, *Corynebacterium glutamicum*, and yeasts[30]. Large-scale production of D-allulose has already been industrialized[31] with a cost of just CNY 20 per kg—~100 times cheaper than IPTG (CNY 2500 per kg). These features make the PsiR–allulose pair an attractive basis for constructing inducible systems. However, the native PsiR suffers from low sensitivity (EC_{50} ≈ 20 mM) and a limited dynamic range[32]. This highlights the need for in-depth engineering of the PsiR-allulose system to enhance its response features. However, it remains a challenge due to the limited knowledge of crystal structure and binding mechanism of PsiR, and even scarce methods for rational design.

In this work, we demonstrate the successful rational design of PsiR and established a flexible framework for allulose-mediated auto-inducible protein expression and autonomous dynamic gene regulation (Fig.1). We first construct a D-allulose-responsive system in *Corynebacterium glutamicum* and systematically optimize the gene expression of PsiR and reporter enhanced green fluorescent protein (eGFP) to ensure robust signal output. Then, we present the structure-guided computational design and engineering of the access-binding-allostery process of PsiR, enabling decreasing the EC_{50} of the resulting PsiR-allulose biosensors (PABs) from 16.7 mM (the wild-type) to 0.8 mM. We further uncover the underlying mechanism and validate the feasibility of the computer-guided tunnel engineering approach to enhance the signal output of LacI, highlighting its broader applicability to other LacI-family TFs. Building upon this, by integrating an allulose biosynthetic pathway and the PsiR-allulose sensor in a single cell, we establish an inducer-free allulose-mediated auto-inducible expression (AMAE) system for mannose isomerase production. In parallel, we develop an allulose-triggered CRISPR interference (CRISPRi) circuit (ATCi) to dynamically repress *zwf*, encoding glucose-6-phosphate dehydrogenase in the pentose phosphate pathway, achieving a higher conversion yield of 0.43 g/g glucose than the traditional enzymatic biotransformation method (0.18 g/g glucose). Collectively, this study provides a versatile allulose-responsive biosensor toolbox and presents a modular framework for developing gene regulation circuits in metabolic engineering and synthetic biology.

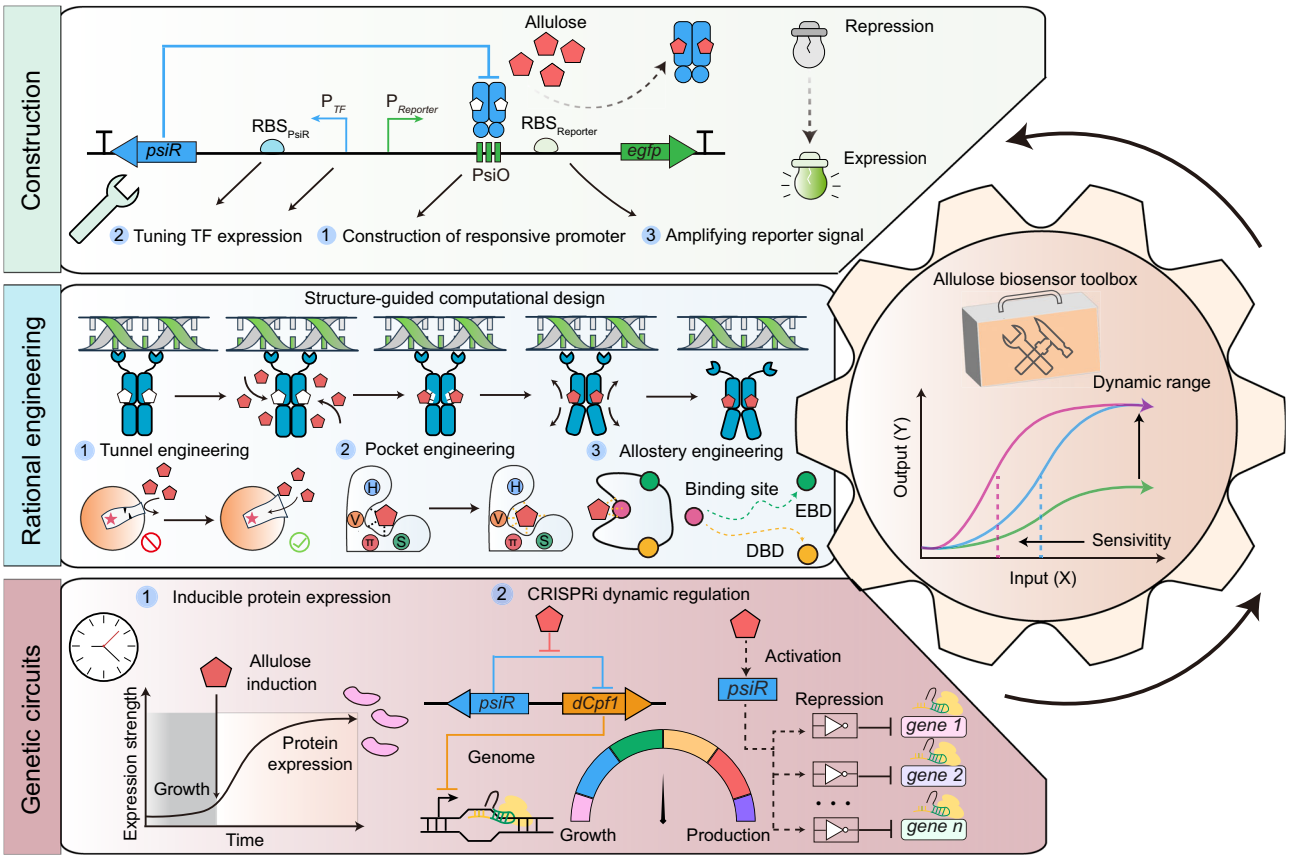

Fig. 1 | Rational design and engineering of allulose-responsive biosensors for protein expression and CRISPR interference (CRISPRi)-mediated dynamic regulation. A PsiR-based allulose biosensor is constructed in *Corynebacterium glutamicum*, rationally optimized through tunnel, pocket and allostery engineering in the effector-binding domain to enhance allulose responsiveness, and implemented in genetic circuits to drive allulose-inducible protein expression and allulose-triggered CRISPRi-mediated dynamic regulation.

https://doi.org/10.1038/s41467-025-67669-6

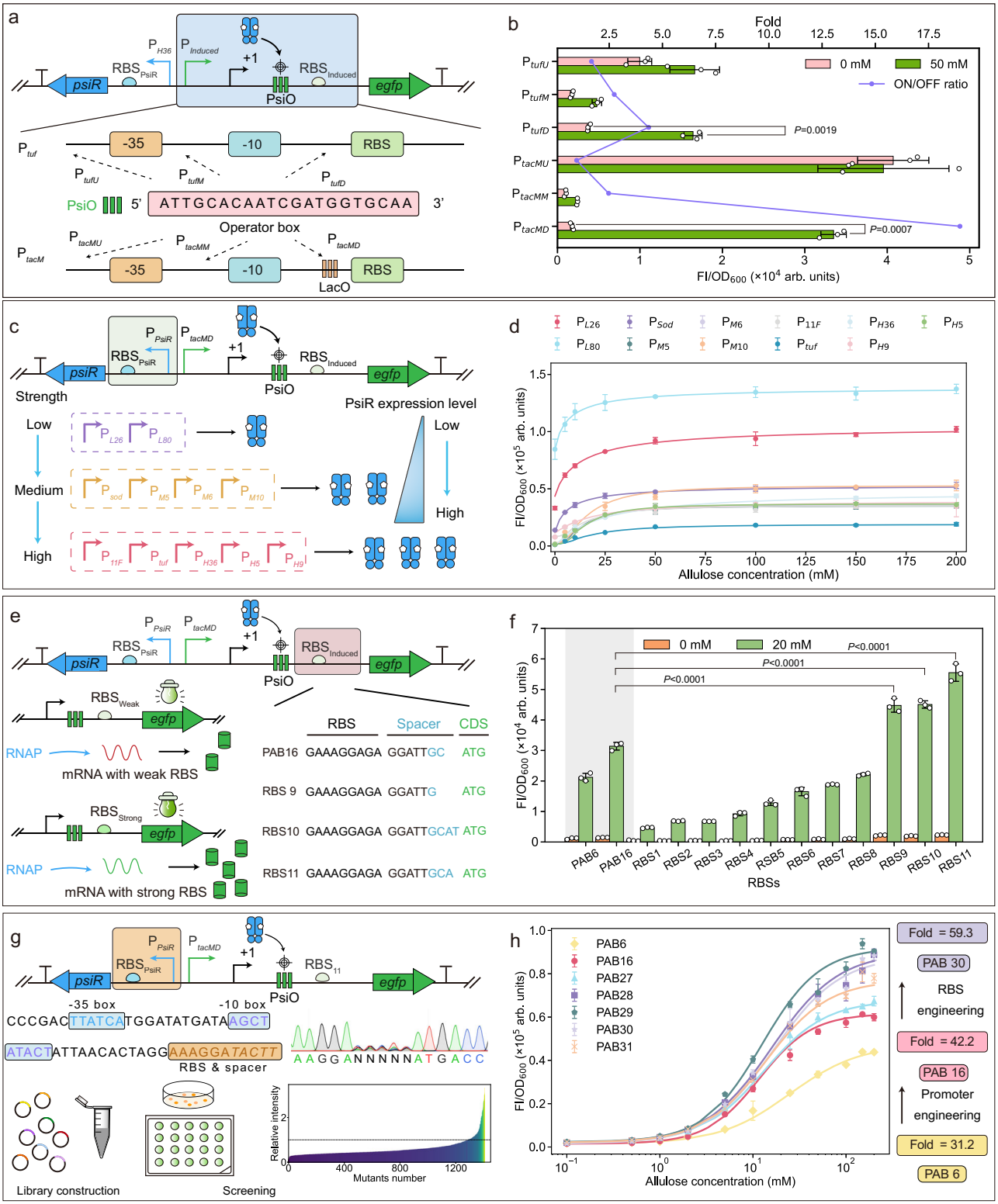

Results

Construction of allulose-responsive biosensors in *C.glutamicum*

Typically, a TF-based biosensor system is composed of two main components: one expression cassette for expression of the TF, and the other containing a TF-binding operator to drive the expression of the reporter gene. In this work, we aimed to construct an allulose-responsive biosensor in *C. glutamicum*. To this end, a constitutive promoter P_{H36} was employed to express the TF PsiR, while a series of hybrid promoters were designed by inserting the PsiR-binding sequence PsiO (ATTGCACAATCGATGGTGCAA) into different positions of the P_{tuf} and P_{tacM} promoters[33] to control the expression of eGFP (Fig. 2a and Supplementary Table 1). The fluorescence output of the resulting biosensors (PABs) was measured in response to varying allulose concentrations ranging from 0 to 200 mM. The results showed that inserting the PsiO sequence between the −10 box and the ribosome binding site (RBS) enabled allulose sensing (Fig. 2b and Supplementary Fig. 1). Among these, PAB6, in which the PsiO replaced the lacO site in the P_{tacM}, exhibited the highest signal-to-noise ratio (19-fold

Fig. 2 | Construction of allulose-responsive biosensors in *C.glutamicum*. **a** Several hybrid promoters were designed by inserting PsiO sequence (ATTGCACAATCGATGGTGCAA) into different positions of P_{tuf} and P_{tacM} promoters for eGFP expression. **b** The fluorescence of PAB1-6 at 0/50 mM allulose. PAB1: P_{tufU}; PAB2: P_{tufM}; PAB3: P_{tufD}; PAB4: P_{tacMU}; PAB5: P_{tacMM}; PAB6: P_{tacMD}. **c** Optimization of PsiR expression using eleven promoters possessing different expression strength. **d** The fluorescence of PAB6-16 from 0 mM to 200 mM allulose. PAB6: P_{H36}; PAB7: P_{L26}; PAB8: P_{L80}; PAB9: P_{sod}; PAB10: P_{M5}; PAB11: P_{M6}; PAB12: P_{M10}; PAB13: P_{11F}; PAB14: P_{tuf}; PAB15: P_{H5}; PAB16: P_{H9}. **e** Optimization of eGFP expression through changing the spacer sequence between RBS and initiation codon ATG of *eGFP*. **f** The fluorescence of PAB17-27 at 0/20 mM. In panel (**f**), the gray shaded region highlights PAB6 and PAB16, which did not undergo RBS replacement and serve as reference biosensors for comparison with RBS1–RBS11. PAB17: RBS1; PAB18: RBS2; PAB19: RBS3; PAB20: RBS4; PAB21: RBS5; PAB22: RBS6; PAB23: RBS7; PAB24: RBS8; PAB25: RBS9; PAB26: RBS10; PAB27: RBS11. The detailed sequence for RBS1-11 was shown in Supplementary Table 2. **g** Optimization of PsiR expression through replacing the spacer sequences (TACTT) between the RBS of P_{M10} and ATG in PAB27 with five random nucleotides (NNNNN). More than 1400 strains were screened under 0/50 mM allulose. Four biosensors PAB28-PAB31 with significant increase in signal output relative to PAB27 were selected for detailed characterization. **h** The detailed Hill equation data of different PABs from 0 mM to 200 mM allulose. Data are presented as mean values +/−SD ($n = 3$ independent experiments). Statistical analysis was performed by two-sided *t* test with Welch's correction (**b**) comparing 0 and 50 mM allulose for each construct, and by one-way ANOVA (**f**) followed by Dunnett's post hoc test using PAB16 as the control to compare PAB17–PAB27 with PAB16. Source data for (**b**, **d**, **f**, **h**) are provided as a Source Data file.

at 0/50 mM allulose). However, its overall fluorescence output remained low, likely due to strong repression of eGFP expression by PsiR. To address this, we fine-tuned PsiR expression using a set of eleven promoters with varying strengths[34] (Fig. 2c and Supplementary Table 2). Indeed, strong promoters such as P_{tuf}, P_{H36}, P_{H9}, and P_{H5} led to the tight repression of eGFP, resulting in low fluorescence even at 200 mM allulose (Fig. 2d). In contrast, weak promoters like P_{L26} and P_{L80} generated higher fluorescence but caused undesirable basal leakage. Notably, PAB16, which used a medium-strength promoter P_{M10} for PsiR expression, increased the maximum fluorescence by 20% compared to PAB6 while maintaining strict repression in the absence of allulose.

To further enhance the dynamic range and signal output, we next optimized PsiR and eGFP expression at the translational level. For eGFP, the RBS of P_{tacMD} in PAB16 was replaced with eleven alternative RBS sequences (Fig. 2e and Supplementary Table 3). PAB27 exhibited a 77% increase in fluorescence output compared to PAB16, while maintaining very low basal leakage expression (Fig. 2f). To refine PsiR translation, we constructed a mutant library by replacing the spacer sequence (TACTT) between the RBS of P_{M10} and initiation codon (ATG) in PAB27 with five random nucleotides (NNNNN) (Fig. 2g). After screening 1,400 strains under 0/50 mM allulose, 78 strains with improved signal output relative to PAB27 were identified. Four biosensors, named as PAB28-PAB31, were selected based on their superior fluorescence fold-change values (Supplementary Figs. 2, 3) and were further characterized across a gradient of allulose concentrations, with their responses were fitted to the Hill equation. Among them, PAB30 exhibited a 30% increase in maximum signal compared to PAB27 while maintaining low background expression. Overall, by systematically optimizing both PsiR and eGFP expression, PAB30 achieved an 86% improvement in maximum fluorescence relative to the initial PAB6. Furthermore, its fluorescence dynamic range reached 59.3-fold, and the EC_{50} for allulose was reduced to 16.7 mM (Fig. 2h and Supplementary Table 4).

Overall structure of PsiR and its binding mode

To date, the crystal structure of PsiR and its binding conformations with allulose and the operator sequence PsiO have remained unknown. To better understand the molecular basis of PsiR, we attempted to determine the full-length crystal structure of the PsiR–allulose complex, but were unsuccessful. Notably, several reported crystal structures of LacI family TFs, such as LacI (PDB: 2P9H), RbsR (PDB: 4RK1), SghR (7CDX), and Cra (PDB: 3O75), lack the N-terminal DNA-binding domain (DBD), which is responsible for DNA recognition. Inspired by the truncated construct of LacI structure (PDB: 2P9H), we introduced an N-terminal truncation in PsiR at Ser69. This strategy enabled us to successfully solve the crystal structure of the PsiR–allulose complex at 2.02 Å resolution using X-ray crystallography (PDB: 9KPR; Supplementary Fig. 4 and Table 5). The overall structure forms a homodimer, with each monomer consisting of a C-terminal core domain that governs both ligand binding and allosteric transitions. Although PsiR shares only 24.8% sequence identity with LacI, it adopts a similar three-dimensional structure similar to that of LacI and other members of the LacI-family TFs (Supplementary Fig. 5).

We have also attempted to reveal the binding model between PsiR and PsiO by solving the complex crystal structure of PsiR-PsiO, but failed. As an alternative, we obtained the complete complex structure based on 9KPR with the aid of AlphaFold3[35] (Fig. 3a). The predicted structural model was quantitatively assessed using two key metrics: i) the root-mean-square deviation (RMSD) of PsiR and DNA converged within 200 ns and remained stable thereafter; and (ii) the center-of-mass (COM) distance between the DBDs and the conserved 20-bp core region of PsiO remained constant (Supplementary Fig. 6). The DBD adopts a helix-turn-helix (HTH) motif and is connected to the core domain via a flexible hinge region (residues 46–66). In the modeled structure, the HTH of PsiR is embedded into the major groove of the PsiO double-stranded DNA. Several polar residues, including S21, S23, R36, R37, R39, R54, and R65, may interact with the PsiO operator sequence (TTGCACCATC) via hydrogen bonds and salt bridges (Fig. 3b). The long-range molecular dynamics (MD) simulation analysis lasting 1 μs revealed that the PsiO operator region maintained high structural stability during the in silico simulation process compared to the flexible HTH domain (Fig. 3c). Upon PsiO binding, PsiR induces a pronounced bend (from 180° to ~130°) in the DNA helix through electrostatic and van der Waals interactions (Fig. 3d and Supplementary Fig. 7), which was consistent with structural features also observed in the LacI-DNA complex[36].

The crystal structure of the PsiR-allulose complex revealed that the allulose is stabilized by forming strong hydrogen bond interactions with surrounding residues, which was further supported by residue–ligand interaction energy analysis (Fig. 3e, f). To validate the functional relevance of these residues, we further conducted alanine-scanning mutagenesis on these residues. Although mutations of P77A, N81A, and F84A retained allulose responsiveness and even enhanced the maximum signal output, their basal leakage also significantly increased relative to wild-type (Fig. 3g). Mutations of F83A, D155A, R208A, Y233A, and D288A completely abolished the allulose response, resulting in an Is phenotype. It indicates that these residues are critical for ligand binding or allosteric signal transmission. In particular, D288 appears to play a crucial role in ligand stabilization through strong hydrogen bonding, as confirmed by saturation mutagenesis at this site (Supplementary Fig. 8). Interestingly, the residues D155, R208, and D288 in PsiR are also conserved in the ligand-binding sites of other carbohydrate-responsive LacI-family TFs, including LacI (PDB: 2P9H), RbsR (PDB: 4RK1), Cra (PDB: 3O75), and CelR (PDB: 5YSZ) (Fig. 3h). Previous studies have shown that mutations at homologous residues, such as D149 residue in LacI and R205 in CelR, could disrupt substrate binding and allosteric transitions[37,38], This indicates that the conserved D–R–D/R triad may play a crucial role in effector binding and allosteric activation within the LacI family TFs.

https://doi.org/10.1038/s41467-025-67669-6

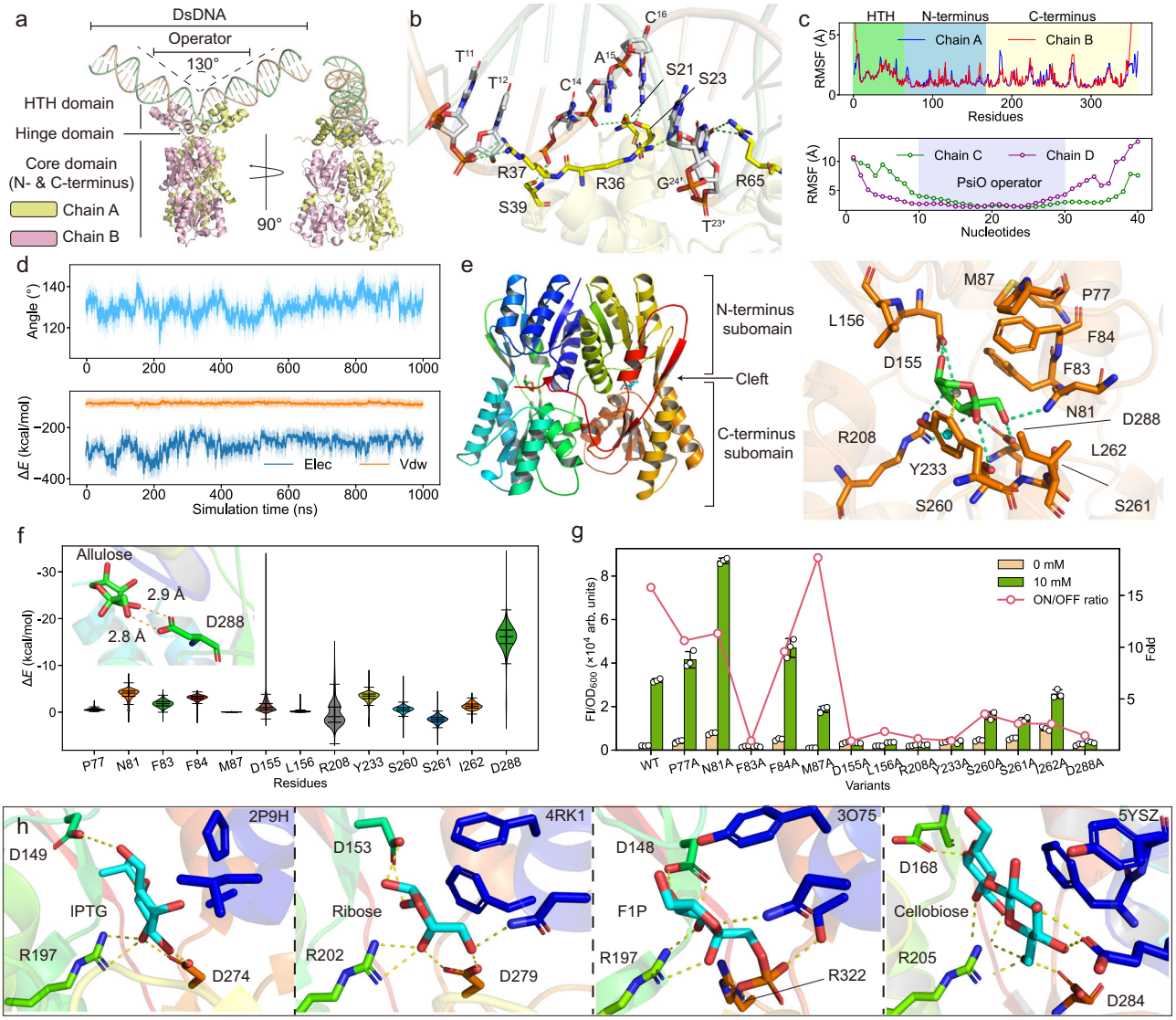

Fig. 3 | Overall structure and binding mode of PsiR with PsiO and allulose. a The overall structure of PsiR and the binding mode with PsiO. The crystal structure of PsiR-allulose complex (PDB ID: 9KPR) was solved, and the PsiR-PsiO complex crystal structure was obtained with the aid of AlphaFold3. **b** The interaction between helix-turn-helix (HTH) of PsiR and the major groove nucleotides of PsiO. **c** The root-mean-square fluctuation (RMSF) data of PsiR-PsiO complex under 1-μs-long range MD simulation. In panel (**c**), the green, blue and yellow shaded regions denote the HTH, N-terminal and C-terminal subdomains of PsiR, respectively, and the purple shaded region in the lower plot marks the 20-bp core PsiO operator within the DNA. **d** The electrostatic interaction and van der Waals interactions between HTH and PsiO. **e** The binding conformation between PsiR and allulose in EBD. **f** Distributions of per-residue interaction energies between allulose and surrounding residues along a 1 μs MD trajectory. For each residue, total residue–allulose interaction energies (ΔE) were calculated every 10 ps, 100,000 frames in total. Violin plots show the kernel density of the per-frame interaction energies; inner boxes indicate the interquartile range (25–75th percentiles) with the center line representing the median, and whiskers denote the most extreme data points within 1.5 × IQR. **g** The fluorescence values and regulatory range (fold) of different PsiR mutants after alanine scanning under 0/10 mM allulose. **h** The ligand-TF binding mode in other LacI-family TFs. The D-R-D/R binding triad is shown. Data are presented as mean values +/−SD ($n = 3$ independent experiments). Source data for (**c**, **d**, **f**, **g**) are provided as a Source Data file.

Computer-aided tunnel engineering of PsiR

It was noted that TFs perform the response function primarily rely on ligand-induced conformational changes and allosteric transitions. The residues involved in such allosteric processes are often distributed throughout the protein structure[16], and untargeted mutagenesis is prone to loss-of-function phenotypes and reduced biosensor performance. Given the currently unknown topological trajectory of the allosteric transition in PsiR, we sought to deconstruct the response process into four sequential steps (Fig. 4a): i) allulose recognition and entry into the EBD; ii) allulose binding to target residues in the EBD and triggering the conformational rearrangement; iii) allosteric transition within EBD and to DBD; iv) dissociation of HTH motif from the PsiO operator, leading to eGFP expression. In this context, the residues acting on those processes may serve as candidates for engineering.

From this framework, we prioritized the engineering of effector access (step i), reasoning that modifying allulose entry access is less likely to perturb the delicate intramolecular allosteric network[17]. Based on the PsiR-allulose complex crystal structure, we analyzed the potential access tunnels using CAVER 3.0[39]. Among the identified tunnels, the tunnel 1(Fig. 4b), comprising residues R109, V134, T135, D155, and D202, exhibited the widest bottleneck radius, lowest curvature, and highest flux, and was therefore considered the primary tunnel for inducer movement. To investigate the interactions between allulose and the tunnel-lining residues during allulose translocation,

https://doi.org/10.1038/s41467-025-67669-6

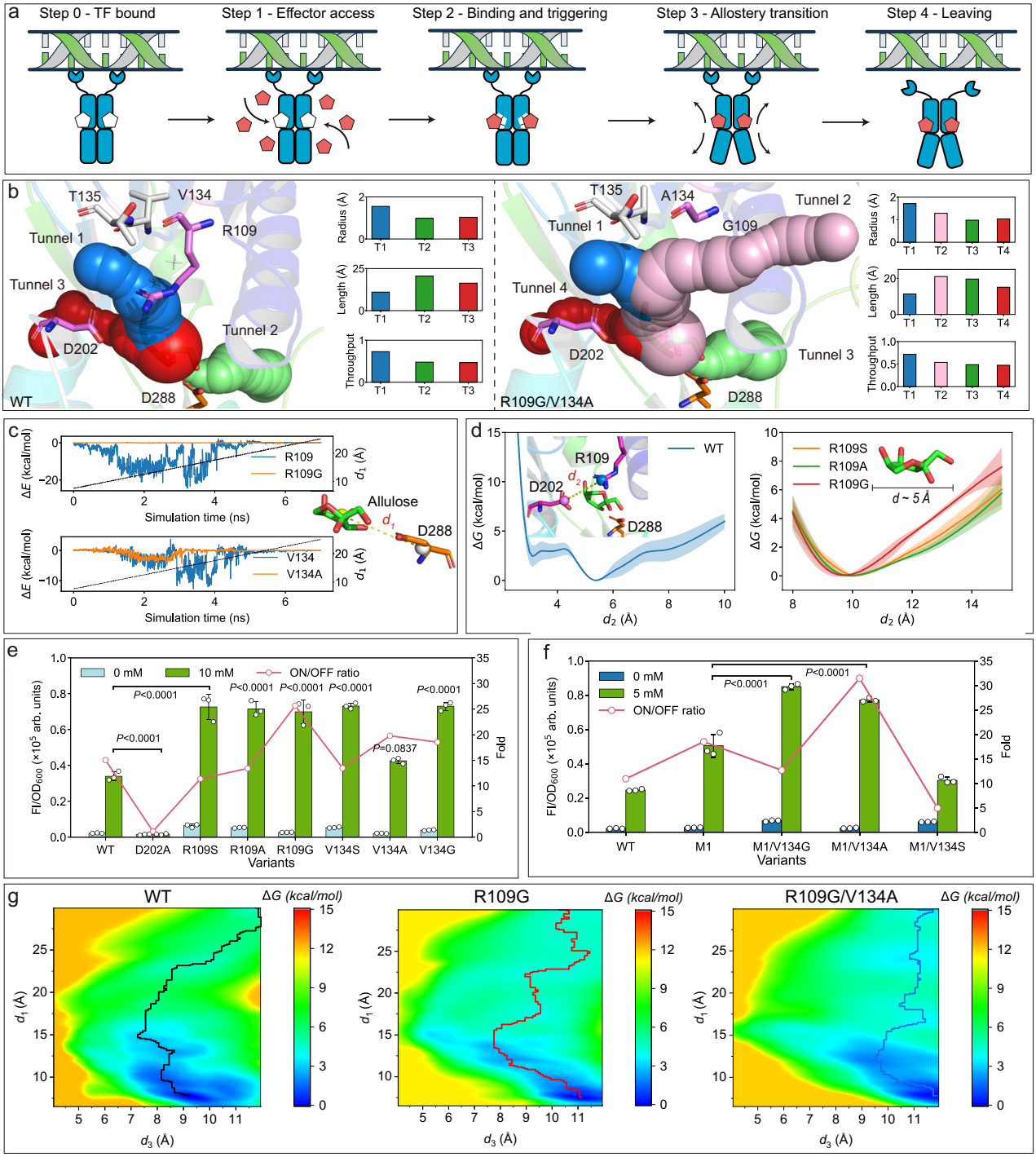

Fig. 4 | Tunnel engineering of PsiR to increase the sensitivity and dynamic range. a Four steps for PsiR response. **b** The potential allulose access tunnels in PsiR calculated by CAVER 3.0. The characteristics of bottleneck diameter, curvature, and flux are shown and compared. The potential allulose access tunnels in PsiR-M2, and the corresponding characteristics are compared. **c** The interaction energy of allulose with R109, V134, R109A, and V134A during SMD simulations. **d** The tunnel bottleneck diameter between sites 109 and 202 of PsiR-WT and mutants R109A, R109S, and R109G. In panel (**d**), the shaded bands around each curve represent the standard deviation calculated from three independent simulations. **e** The fluorescence values and regulatory range (fold) of different single-site PsiR mutants for 109 and 134 sites under 0/10 mM allulose. **f** The fluorescence values and regulatory range (fold) of combinatorial double mutants under 0/5 mM allulose. **g** The two-dimensional well-tempered metadynamics–extended-system adaptive biasing force (WTM-eABF) free energy of allulose access to the binding site for WT, R109G, and M2. The center-of-mass distance between allulose and D288 (d_1) was defined to indicate the allulose entrance, and the center-of-mass distance between R109G or G109 and allulose (d_2) was defined to indicate the interaction between allulose and R109. Data are presented as mean values +/−SD ($n = 3$ independent experiments). Statistical analysis for panels (**e**) and (**f**) was performed by one-way ANOVA followed by Dunnett's post hoc test (using WT as the control in (**e**) and M1 as the control in (**f**); P values are indicated in the panels. Source data for (**b**–**g**) are provided as a Source Data file.

steered molecular dynamics (SMD) simulations were conducted by applying a pulling force to guide allulose from the EBD along the predefined tunnel 1. A collective variable, d_1, was defined as the COM distance between allulose and the key active-site residue D288. The interaction energies (ΔE (kcal/mol)) between allulose and individual residues along the route were calculated to identify potential hotspot residues (Supplementary Fig. 9). The D155, a conserved component of the D–R–D triad critical for effector recognition in LacI-family TFs (Fig. 3h), was excluded from engineering targets. Residues R109 and D202 displayed strong interaction energies with allulose during the SMD process (Fig. 4c, Supplementary Fig. 9), likely due to their long polar side chains and the formation of salt bridges in the crystal structure (Fig. 4d). Such strong interaction between these two residues would hinder ligand movement through the tunnel. To reduce steric hindrance and electrostatic barriers, we performed in silico mutagenesis of R109 to smaller and less charged residues (Ala, Ser, Gly) and analyzed the interaction energies after SMD simulations (Fig. 4c, Supplementary Fig. 10). To monitor the salt bridge interaction between R109 and D202 during allulose translocation for PsiR-WT and its mutants, the collective variable, d_2, was defined as the COM distance between the carboxyl group of D202 and guanidyl group of R109. These substitutions significantly reduced interaction energies and expanded the tunnel bottleneck diameter from 5–6 Å to ~10 Å (Fig. 4d), thereby lowering the free energy barrier and increasing the possibility for allulose entry. Experimental validation revealed that R109A substantially enhanced biosensor responsiveness to 10 mM allulose (Fig. 4e). Notably, mutants R109S and R109G not only improved the maximal fluorescence signal but also reduced basal leakage compared to R109A. Relative to wild-type PsiR, the R109G variant doubled the fluorescence output and increased the dynamic range (fold change) by 64% to 25.7 under 0/10 mM allulose. In contrast, while the D202A mutant exhibited tight repression in the absence of inducer, it failed to respond to allulose, suggesting that D202 may participate in allosteric transition. Collectively, these findings demonstrate that rational remodeling of the ligand entry tunnel—particularly via modulation of salt-bridge-forming residues—offers an effective strategy to fine-tune biosensor sensitivity and dynamic range.

Encouraged by the improved sensor performance of R109G, we next investigated another tunnel-lining residue, V134, which also displayed high interaction energy with allulose in SMD simulations (Fig. 4c). Mutagenesis at this site—V134A, V134S, and V134G—led to a consistent enhancement in both signal output and dynamic range compared to the wild-type PsiR (Fig. 4e). Notably, V134A conferred the highest on/off ratio, while V134G yielded the strongest fluorescence signal under 10 mM allulose. To further amplify sensor sensitivity at lower inducer concentrations, we combined R109G with these beneficial V134 variants. Among the resulting double mutants, the R109G/V134A combination (designated M2) demonstrated very low basal leakage expression in the absence of inducer, alongside improved allulose responsiveness compared with that of R109G under a lower allulose concentration of 5 mM (Fig. 4f). Specifically, M2 achieved a dynamic range of 31.5-fold at 0/5 mM allulose, representing a 2.9-fold enhancement relative to the wild-type.

Further structure analysis revealed that T135 is located at the entrance of the primary access tunnel, functioning as a gating residue that potentially influences ligand recruitment (Supplementary Fig. 11a, b). SMD-based interaction analysis in both WT and M2 backgrounds confirmed strong interaction energies between T135 and allulose (Supplementary Fig. 11c), suggesting its critical role in tunnel accessibility. To alleviate this bottleneck, saturation mutagenesis of T135 was performed in the M2 background. While substitutions with small residues (Ala, Ser, Gly) increased signal output at 5 mM allulose, they also significantly elevated background leakage in the absence of allulose (Supplementary Fig. 12). In contrast, bulkier substitutions (Met, Tyr, His, and Arg) at position 135 in variants M2-T135M, M2-T135Y, M2-T135H, and M2-T135R maintained lower background noise compared to M2. Among them, M2-T135H achieved a dynamic range (fold-change at 0 vs. 5 mM allulose) of 52, surpassing that of M2. However, this enhancement in regulation was accompanied by a 31% reduction in signal output relative to M2 (Supplementary Fig. 12).

To elucidate the evolution of enhanced sensitivity and dynamic range of M2, we employed two-dimensional well-tempered metadynamics-extended adaptive biasing force (WTM-eABF) simulations. This approach is effective for resolving multidimensional and rugged free energy landscapes and has been successfully applied to investigate dynamic processes, including glucan–enzyme interactions and protease catalysis[40–42]. To characterize the free energy landscape associated with allulose translocation, we introduced the third collective variable, d_3, defined as the distance between allulose and residue R109, which reflects the local interaction strength at this key engineering site. Concurrently, the collective variable, d_1, was used to monitor the distance between allulose and D288, capturing its dissociation path from the binding site to the solvent-exposed state. Based on these variables, we computed and compared the two-dimensional free energy landscapes (ΔG (kcal/mol)) as functions of d_1 and d_3 for PsiR-WT, PsiR-M1 and PsiR-M2 (Fig. 4g). Free energy surfaces were derived from >600 ns of simulation per variant. As expected, R109G significantly broadened the low-energy region and reduced the energetic barrier for allulose access by 1.49 kcal/mol (Supplementary Fig. 13). By comparing the highlighted least free-energy routes, the interaction between R109G and allulose decreased, resulting in a rightward shift far away from R109, confirming the reduced local constraint. Further incorporation of V134A in M2 lowered the post-R109 barrier, suggesting a smoother transition from entry to binding. Therefore, the enhanced sensing characteristics of M2 may be due to the reduced interaction barrier in the allulose access. In addition, more access tunnels were discovered for mutant PsiR-M2 (Fig. 4b), allowing the mutated PsiR to be triggered at lower allulose concentrations.

Computer-aided tunnel engineering of LacI

Our results demonstrate the feasibility of computer-aided tunnel engineering for enhancing sensor sensitivity, signal output, and dynamic range of PsiR through the screening of a focused mutational library. To assess the generalizability of this strategy across the LacI transcription factor family, we applied the same approach to engineer LacI for improved signal output and sensitivity. We first constructed a LacI-based eGFP reporter sensor in *C. glutamicum*. Then, the SMD simulations were performed by pulling IPTG along the most likely tunnel pathway, and interaction energies between IPTG and individual tunnel-lining residues were analyzed (Supplementary Fig. 14). This identified five residues of D149, N125, S101, S69, and S70 exhibiting strong interactions with IPTG. The D149 and N125 were excluded from mutagenesis due to the conserved D–R–D/R triad in ligand binding and allosteric regulation[37]. To reduce steric and electrostatic hindrance at R101, we substituted it with smaller residues (Ala, Gly, Ser). Among these variants, the R101A and R101S mutants exhibited a 2–3 fold increase in fluorescence output at 10 μM IPTG compared to the wild-type LacI (Supplementary Fig. 15).

Further analysis revealed that residues S69 and S70, located at the entrance of the access tunnel, also interact with IPTG. Since these positions are already occupied by the small amino acid serine, we performed saturation mutagenesis to comprehensively explore potential improvements at these sites. Eighteen mutants increased the signal output by 2.0–4.8 fold (Supplementary Fig. 16). Among these, the mutant S70M yielded the highest output but exhibited elevated basal leakage in the absence of IPTG. In contrast, the S69C, S70T, and S70N maintained a low basal leakage level comparable to that of the wild-type, while still achieving 2–3.2 fold enhancement in signal output. Furthermore, those four beneficial single mutants (R101S, S69C, S70T, and S70N) were further characterized across a gradient of IPTG

https://doi.org/10.1038/s41467-025-67669-6

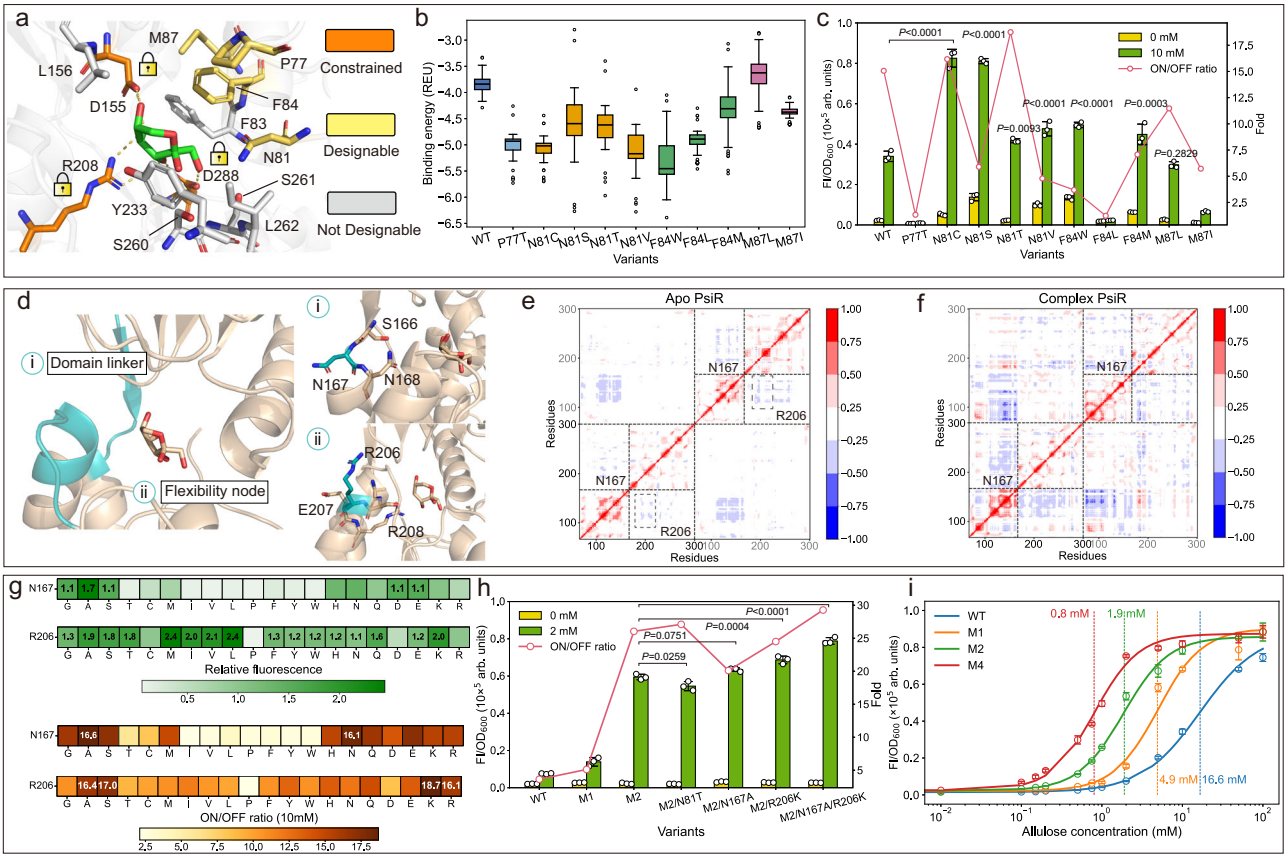

Fig. 5 | Engineering the binding pocket and allosteric sites to increase the sensitivity and dynamic range. a The amino acids of P77, N81, F84, and M87 in the EBD. **b** Box plots showing the distributions of Rosetta binding energy scores (REU) for wild-type PsiR and designed variants. For each variant, $n = 200$ independently generated design models were evaluated in silico. Center line, median; box limits, 25–75th percentiles; whiskers, most extreme data points within 1.5×interquartile range; points denote outliers. **c** The fluorescence values and regulatory range (fold) of single-site mutants for P77, N81, F84, and M87 under 0/10 mM allulose. **d** The junction region connecting the N-terminal and C-terminal subdomains and the rigid helix region (residues 204-208) in core domain. The residues of N167 and R206 were located in this area. **e** The dynamic cross-correlation matrices of apo PsiR. **f** The dynamics cross-correlation matrices data of PsiR-complex. **g** The fluorescence relative to PsiR-WT and regulatory range (fold) under 0/10 mM for the saturation mutagenesis mutants of N167 and R206. **h** The fluorescence values and regulatory range of different single-site and combinatorial mutants under 0/2 mM allulose. **i** The detailed Hill equation data of PABs possessing different PsiR mutants from 0 mM to 100 mM allulose. Data are presented as mean values +/−SD ($n = 3$ independent experiments). Statistical analysis for panels (**e**) and (**f**) was performed by one-way ANOVA followed by Dunnett's post hoc test; *P* values are indicated in the panels. Source data for (**b**, **c**, **g**, **h**, **i**) are provided as a Source Data file.

concentrations, with their responses were fitted to the Hill equation (Supplementary Figs. 15b, 16b, d). The results confirmed the increased dynamical range and sensitivity of engineered mutants relative to wide-type. These findings further validate the utility of computational tunnel engineering as a generalizable strategy for tuning ligand sensitivity in LacI-family transcriptional biosensors.

Rational engineering of binding pocket and allosteric sites

After alleviating the steric restriction in the allulose access tunnel, we then attempted to rationally engineer key residues involved in ligand binding in EBD and allosteric transition from EBD to DBD (Fig. 4a). It was suggested that enhancement of allulose binding via a suitable conformation in the binding pocket would generate more robust triggering response ability. According to our alanine scanning results in EBD, residues P77, N81, F84, and M87 may be less conserved in PsiR (Fig. 3g). Therefore, using Rosetta-based protein design, we computationally redesigned these positions and selected 11 single-point mutants with improved interface binding energies (Fig. 5a, b). Functional assays revealed that seven variants exhibited a 1.2- to 2.4-fold increase in fluorescence response under 10 mM allulose compared to the wild-type sensor (Fig. 5c). Notably, the N81T mutation not only enhanced the signal output by 23% and expanded the regulatory dynamic range (from 15.1 to 18.8), but also preserved a low basal expression level, making it a promising candidate for further biosensor development.

Effector binding at the EBD allosterically triggers the dissociation of PsiR from its operator site (PsiO), yet the structural basis for topological propagation from the EBD to the distant DBD—particularly across the hinge and helix-turn-helix (HTH) motifs—remains unclear but is meaningful to explore. To investigate this long-range communication, we performed long time-scale MD simulations of the PsiR–allulose complex and applied principal component analysis (PCA) to the Cα atom trajectories of the homodimer (Supplementary Fig. 17). The dominant conformational changes centered in the loop between β4–β5 and helices α6–α7 within the EBD's N-terminal subdomain, the helices α10–α11 in the C-terminal subdomain, as well as the junction regions (166–168) between the N-terminal and C-terminal subdomains. These dynamic regions may serve as structural conduits for allosteric transition, mediating the conformational switch required for PsiR function.

To further elucidate the intramolecular interaction landscape within PsiR, we computed dynamic cross-correlation matrices (DCCMs) for both apo and allulose-bound states[43]. In the absence of ligand, strong positive correlations were primarily confined within each of the N- and C-terminal subdomains, while weak inter-subdomain anticorrelated motions were observed (Fig. 5d–f). Upon

allulose binding, the internal correlations within the N-terminal subdomain were further strengthened, accompanied by a marked increase in dynamic anticorrelations between the N- and C-terminal subdomains. These changes indicate a more coordinated and functionally relevant dynamic shift upon ligand binding. Notably, dynamic correlations for N- and C-terminal subdomains were separated at the junction region, suggesting it serves as a critical conduit for allosteric transmission. Based on this observation, residue N167 at the domain interface was selected for saturation mutagenesis.

In a hydrogen–deuterium exchange mass spectrometry (HDX/MS) study, Glasgow et al. systematically profiled allosteric conformational changes across the full core domain of LacI[44–46]. Their analysis revealed increased structural rigidity in several regions adjacent to the ligand-binding pocket in the IPTG-bound state compared to the DNA-bound state, suggesting these segments as potential hotspots for allosteric engineering. Through structural alignment of PsiR with LacI, we identified a corresponding segment (residues G199–R206 in PsiR; homologous to G187–R195 in LacI) located near the allulose-binding site within the C-terminal subdomain (Supplementary Fig. 18). Furthermore, root-mean-square fluctuation (RMSF) analysis revealed greater stability in this region under the PsiR–allulose state compared to the PsiR–DNA binding mode (Supplementary Fig. 19). However, residue R206 exhibited increased flexibility relative to surrounding residues. To enhance the local rigidity of this segment, we conducted saturation mutagenesis at position R206.

Experimental screening of these mutants revealed that substitutions N167A and N167S both enhanced signal intensity and dynamic range compared to the wild-type. Several R206 variants also showed improved performance, among which R206K notably doubled the fluorescence signal and improved the regulatory fold by 16%, while maintaining minimal background noise (Fig. 5g). Conversely, substitution of R206 with proline abolished activity, highlighting the importance of maintaining a certain flexibility at this site. The results emphasize the importance of the junction region of the N- and C-terminal subdomains and its role as an allosteric transmission conduit, offering an effective target for enhancing biosensor performance.

Next, we combinatorially introduced the beneficial single-site mutants of N81T, N167A, and R206K into M2 and evaluated its performance at a reduced allulose concentration (2 mM). Among the resulting tri-mutant variants, mutants R109G/V134A/N167A (M3) and R109G/V134A/R206K showed the increased signal output relative to M2 (Fig. 5h). Mutation of R109G/V134A/N81T did not have positive effect in improving the fluorescence intensity. Ultimately, combining R206K and N167A in the M2 background yielded mutant M4 (R109G/V134A/N167A/R206K), which exhibited superior performance in the signal output and dynamic range. Specifically, M4 demonstrated a 10-fold enhancement in fluorescence output—from ~7700 (WT) to ~77,000—and an expanded regulatory fold from 3.6-fold to 29-fold in the absence versus presence of 2 mM allulose. We further fitted the fluorescence responses of the various mutants to the Hill equation to estimate their respective EC_{50} values (Fig. 5i). Hill curve fitting revealed that PAB30(PsiR-M4) had a significantly reduced EC_{50} of 0.8 mM, representing an ~20-fold improvement in sensitivity compared to the wild-type PAB30(PsiR) (EC_{50} = 16.6 mM).

To biochemically validate these findings, we performed electrophoretic mobility shift assays (EMSAs)[47] and microscale thermophoresis (MST)[48] to analyze the DNA–PsiR and allulose–PsiR binding interactions. After purifying PsiR-WT, M2, and M4 from *E. coli* BL21(DE3) via His-tag affinity chromatography (Supplementary Fig. 20), both EMSA and MST confirmed specific binding between PsiR and its ligands (Supplementary Fig. 21). Notably, PsiR-M4 exhibited allulose binding at lower concentrations than the WT and M2 (Supplementary Fig. 22), corroborating its enhanced sensitivity. Substrate specificity profiling of the PsiR-WT and PsiR-M4-based sensors against 12 sugars—including seven ketoses (D-allulose, D-fructose, D-sorbose, L-fructose, D-tagatose, D-ribulose, D-xylulose), four aldoses (D-allose, L-rhamnose, L-arabinose, D-xylose), and one sugar alcohol (D-allitol)—demonstrated that the WT sensor responded exclusively to D-allulose at 20 mM substrate concentration (Supplementary Fig. 23). In contrast, the PsiR-M4-based system not only showed enhanced response to D-allulose but also exhibited increased sensitivity to D-sorbose, D-ribulose, D-allose, and D-allitol. Nevertheless, the signals elicited by these non-cognate substrates remained substantially lower than that induced by the native effector, D-allulose.

Design of allulose-responsive gene circuit for enzyme preparation

In this work, we constructed a versatile allulose-responsive genetic circuit platform in *C. glutamicum* using eGFP as a reporter, exhibiting tunable sensitivity, dynamic range, and signal output. To extend its utility beyond biosensing toward practical applications in biomanufacturing, we developed an allulose-inducible expression system for recombinant enzyme production (Fig. 6a). As a proof of concept, we selected D-mannose isomerase (MI), an enzyme that catalyzes the isomerization of D-fructose to D-mannose[49], due to its industrial relevance in mannose biosynthesis. Then, the MI gene from *Thermobifida halotolerans* (ThMI) was used to replace the eGFP in both PAB30-WT and PAB30-M4 circuits (Supplementary Table 6). The resulting strain, designated strain CgWT-MI and CgM4-MI, were cultivated in CGXII minimal medium supplemented with 10 g/L glucose and induced with 5 mM allulose (Fig. 6b). After 24 h of fermentation, strain CgM4-MI achieved an MI activity of 38 U/mL at the shake flask level, representing a fivefold increase over the wild-type circuit (7.6 U/mL), underscoring the potential of the improved PAB30-M4 circuit for high-efficiency enzyme production.

Recently, autoinduction protein expression systems that do not require costly or toxic external inducers have attracted great attention[50]. Inspired by this concept, we proposed a self-regulated expression circuit that leverages intracellularly synthesized allulose as an endogenous trigger. As the cell grows, intracellular allulose levels would gradually increase, thereby activating PsiR-mediated gene expression and enabling allulose-mediated auto-inducible protein expression (AMAE) with no need to supplement of inducer allulose (Fig. 6c). To realize this strategy, we introduced a heterologous allulose biosynthetic pathway branching from the glycolytic intermediate fructose-6-phosphate (F6P). The pathway consisted of allulose-6-phosphate 3-epimerase (AlsE), which catalyzes the reversible epimerization of F6P to allulose-6-phosphate (A6P), and allulose-6-phosphate phosphatase (A6PP), which dephosphorylates A6P to yield free allulose. Thus, microbial synthesis of allulose from glucose could be achieved. For pathway construction, the AlsE and one phosphatase YniC from *E. coli* were co-expressed in *C. glutamicum*. The resulting strain produced 10 mM (1.8 g/L) allulose from 10 g/L glucose within 12 h (Fig. 6d). Notably, the intracellular allulose concentration reached ~5 mM by 6 h of cultivation, aligning with the optimal activation range of PsiR-M4. Based on this observation, we introduced this allulose synthetic pathway into strain CgM4-MI, resulting in AutoCgM4-MI. This strain successfully achieved an MI activity of 25 U/mL after 18 h of cultivation in CGXII medium without the addition of any external inducer (Fig. 6d). The results demonstrate the feasibility of the demonstrated ALAE system for dynamic, self-regulated production of proteins.

Application of PsiR biosensor for dynamic metabolic regulation

Encouraged by the established allulose-inducible expression systems, we next sought to expand the functionality of the PsiR-based biosensor toward dual-directional gene regulation. Specifically, we designed an allulose-triggered CRISPR interference (CRISPRi) circuit (ATCi) to enable programmable gene repression in response to intracellular allulose accumulation (Fig. 7a). In this system, the PsiR-M2 variant

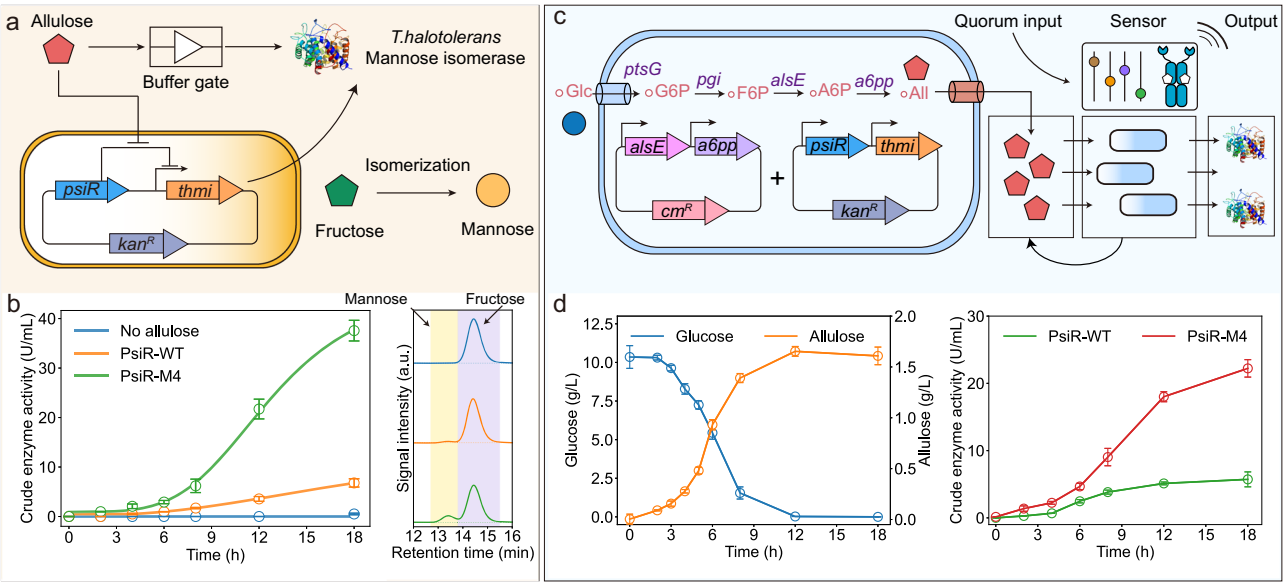

Fig. 6 | Engineering allulose-responsive circuit for enzyme production. a The schematic diagram of the designed allulose-induced expression system for ThMI production. **b** The crude enzyme activity of ThMI in CgWT-MI and CgM4-MI strains. The inducer concentration was 5 mM. **c** The schematic diagram of allulose-mediated autoinduction expression system (AMAE) for ThMI production. **d** The glucose consumption and allulose synthesis in strain AutoCgM4-MI. Also, the ThMI production in AutoCgWT-MI and AutoCgM4-MI was compared. Data are presented as mean values +/−SD ($n = 3$ independent experiments). Source data for (**b**) and (**d**) are provided as a Source Data file.

instead of PsiR-M4 was employed to tightly control the expression of catalytically inactive dCpf1 in designed ATCi circuit, ensuring minimal leaky expression in the absence of allulose and robust induction upon its presence. To implement this architecture, we initially replaced the eGFP with dCpf1 in PAB30-M2, and then chromosomally integrated the expression cassettes containing P_{tacMD}-*dCpf1* and P_{M10}-*PsiR-M2* into the *C. glutamicum* 13032 genome, yielding the engineered strain CgdC-M2 (Supplementary Table 7). In this strain, dCpf1 expression is activated by allulose to regulate target gene expression with the aid of the designed gRNAs. To validate the functionality of ATCi, we constructed a dual-reporter system in CgdC-M2 by integrating constitutively expressed eGFP and mRFP1 under the strong P_{H9} promoter, resulting in strain CgdC-M2-GR. Plasmids carrying gRNAs targeting various regions of eGFP and mRFP1 were introduced separately into strain CgdC-M2-GR. Upon addition of 5 mM allulose, fluorescence signals from both reporters decreased by over 80% (Fig. 7b), confirming efficient and specific gene repression. Furthermore, simultaneous repression of both targets was achieved by co-expression of dual gRNAs. These results demonstrate the feasibility of ATCi for tunable gene silencing in microbial systems.

To explore its utility in metabolic engineering, we applied ATCi to the development of an allulose-producing cell factory (Fig. 7c). We have constructed an allulose synthetic pathway in *C. glutamicum*; however, the resulting strain CgAll1 achieved low titer (8.7 g/L) and yield (0.17 g/g glucose) (Fig. 7d–g), primarily due to competition for carbon flux between cell growth and allulose synthesis. Therefore, we adopted a systematic metabolic engineering strategy to enhance F6P accumulation and enable dynamic regulation of central metabolism. To achieve this end, we constructed a strain CgPIG via the following steps (Fig. 7c): (i) knockout of *pfkA*, encoding 6-phosphofructokinase responsible for converting F6P to fructose-1,6-bisphosphate, thus reducing F6P consumption by the cell; (ii) mutation of the IolR-binding site in the promoter of glucose/myo-inositol permease IolT1 to enhance glucose uptake[51]; and (iii) simultaneous knockout of the *ldhA* gene and chromosomal integration of glucokinase (GlcK) and glucose-6-phosphate isomerase (Pgi) from *Bacillus subtilis* at the *ldhA* locus to boost the supply of glucose-6-phosphate (G6P) and F6P. After introducing the synthetic plasmid (pEC-AlsE-YniC) into strain CgPIG, the resulting strain CgAll2 produced 16.7 g/L allulose, a 1.9-fold improvement over CgAll1 (Fig. 7f).

Previous transcriptome analysis showed that inactivation of *pfkA* would shift carbon flux toward the pentose phosphate pathway (PPP), leading to the upregulation of multiple enzymes in this pathway, including *zwf* (introducing metabolic flow into the PPP)[52]. Since the PPP plays a critical role in NADPH generation and redox balance, the knockout of *zwf* is not feasible. To redirect the carbon flux to allulose synthesis while minimizing the impact on initial cell growth, we employed our designed ATCi system to dynamically regulate *zwf* expression in CgAll2. To this end, the expression cassette of P_{tacMD}-*dCpf1* and P_{M10}-*PsiR-M2* and *zwf*-targeting crRNA were integrated into the genome of CgPIG, resulting in strain CgPIG-dC-M2. Subsequent transformation with pEC-AlsE-YniC generated the production strain, CgAll3. During fermentation, the gradually accumulated endogenous allulose along with cell growth would activate dCpf1 expression, which in turn repressed *zwf* expression, thereby shifting carbon flux toward allulose synthesis. According to the mRNA concentration data (Supplementary Fig. 24), the gene *zwf* expression level was repressed in CgAll3 relative to that in CgAll2. As a result, CgAll3 produced 21.4 g/L allulose after 30 h of fermentation, which was 68% higher than that of the CgAll2 strain (Fig. 7d–g). Also, a conversion yield of 0.43 g/g glucose was achieved for strain CgAll3. The post-30-h decrease in allulose yield (Fig. 7c) is likely due to its reverse isomerization to fructose by the *E. coli* AlsE[53], with the fructose being consumed for growth (Fig. 7a). Addressing this requires AlsE variants with high F6P-to-A6P conversion activity but low reverse activity toward allulose.

Discussion

With the rapid accumulation of bioinformatics data, an increasing number of transcription factors (TFs) are being identified and repurposed for synthetic biology applications. How to fit their response characteristics to meet the demands of specific biomanufacturing scenarios remains a challenge. Many research works focused on tuning the gene expression of TF and reporter through promoter and RBS

https://doi.org/10.1038/s41467-025-67669-6

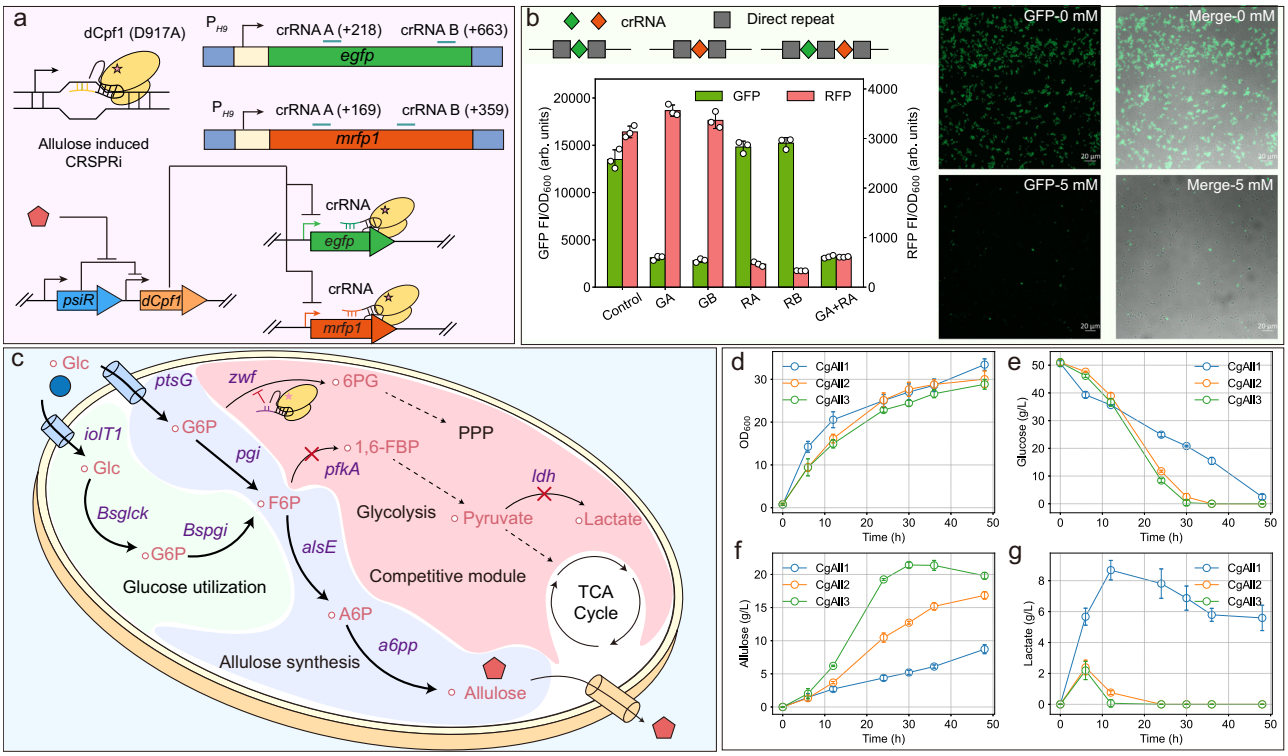

Fig. 7 | PsiR-mediated gene expression repression and dynamic metabolic regulation. a The schematic diagram of the designed allulose-triggered CRISPR interference (ATCi) for regulating gene expression. **b** The verification of our designed ATCi for repressing *eGFP* and *mRFP1* expression in *C. glutamicum* chromosome. G-rA: CgdC-M2-GR (pXMJ19-crRNA-eGFP218); G-rB: CgdC-M2-GR (pXMJ19-crRNA-eGFP663); R-rA: CgdC-M2-GR (pXMJ19-crRNA-mRFP169); R-rB: CgdC-M2-GR (pXMJ19-crRNA-mRFP359); G-rA+R-rA: CgdC-M2-GR (pXMJ19-crRNA-eGFP218-mRFP169). Also, the confocal images of strain CgdC-M2-GR (pXMJ19-crRNA-eGFP218) from the green channel (515–564 nm) under 0 and 5 mM allulose were shown. **c** Metabolic engineering strategy for engineering the allulose synthetic cell factory. Glc Glucose, G6P glucose-6-phosphate, F6P fructose-6-phosphate, A6P allulose-6-phosphate, 1,6-FBP D-fructose 1,6-bisphosphate, 6PG glucono-1,5-lactone 6-phosphate, *BsglcK glcK* from *Bacillus subtilis*, *Bspgi pgi* from *Bacillus subtilis*. **d**–**g** The cell growth (OD_{600}), glucose consumption, allulose synthesis, and lactate synthesis for the strains CgAll1, CgAll2, and CgAll3. Data are presented as mean values +/−SD ($n = 3$ independent experiments). Source data for (**b**–**d**–**g**) are provided as a Source Data file.

engineering[54]. However, such a strategy has a limited effect on improving the sensitivity and ligand specificity, because the native binding model and allosteric transition of TF have not been changed. Here, we presented the structure-guided computational design of access, binding, and allostery process of PsiR in an integrated way. We successfully increased the sensitivity (EC_{50}) of PsiR by 20-fold by screening fewer than 100 mutants and enabled strong activation at low allulose concentrations of 2 mM (Fig. 5i). By integrating structural modeling and molecular simulations, the underlying DNA-PsiR and allulose-PsiR binding mechanism were also elucidated. Meaningfully, such approach delivered an allulose-responsive PAB box with detection range spanning from 10 μM to 100 mM allulose and maximum dynamic range up to 50-fold. These PABs lay the foundation for developing PsiR-based genetic circuits and demonstrate potential for high-throughput screening of beneficial allulose-3-epimerases and aldolases for D-allulose synthesis[55,56]. In this study, a computational framework through analyzing interaction energies, identifying hotspot residues, guiding focused mutagenesis, and elucidating underlying mechanism was introduced in tunnel engineering of PsiR. The proposed tunnel engineering strategy was also successfully extended and verified in engineering the LacI TF, where several engineered variants showed enhanced output at lower IPTG concentrations relative to the wild-type (Supplementary Figs. 15, 16), indicating more efficient IPTG-LacI biosensor for biotechnology application in future[57]. Overall, the computer-aided design of access tunnel, effector binding, allostery transition, even DNA-TF binding would provide a promising and generalizable approach for TFs engineering to improve the sensing property.

Inducible protein expression systems are essential tools in synthetic biology, widely used in industrial enzyme production, biocatalysis, and recombinant pharmaceutical protein manufacturing[18–20]. However, many commonly used systems rely on high concentrations of metabolizable or costly inducers, limiting their applicability. In this work, we established a tightly regulated allulose-inducible protein expression system using the engineered PsiR, functioning at low inducer concentrations (0.5–0.9 g/L), which was comparable with the reported L-arabinose and rhamnose-inducible expression system (0.8–1.5 g/L) but lower than that of maltose (5–20 g/L) and xylose (10–20 g/L) activated system[26–28,58]. This system was successfully applied to MI production, confirming its practical utility. Unlike conventional inducers, allulose is non-metabolizable, food-safe, low-cost, and free from carbon catabolite repression effect[30], enabling robust and sustained induction in the long-term fermentation phase. Together, the advantageous properties of allulose and the tunable responsiveness of PAB sensors make this system a promising platform for safe and efficient recombinant protein expression.

Notably, we developed an inducer-free allulose-mediated autoinducible protein expression (AMAE) system by co-expressing the allulose biosynthetic pathway and a PsiR-based PAB module in a single cell. As glucose was consumed and biomass accumulated, endogenously produced allulose gradually induced target gene expression. Unlike constitutive promoters, AMAE enables a growth-dependent induction profile, reducing metabolic burden during early growth[59]. Moreover, allulose released by individual cell can diffuse and activate gene expression in neighboring cells, forming a self-synchronized, population-wide induction mechanism[60]. Here, we only demonstrated

the application of AMAE using the mutant PsiR-M4; other PsiR mutants in our developed PAB box could also be constructed in AMAE, demonstrating more flexible application potential for protein expression. To extend the application of designed PsiR mutants, we have also constructed the allulose-responsive biosensor in *E. coli* and confirmed the response sensitivity to allulose (Supplementary Fig. 25). In future, the demonstrated allulose-mediated expression system could be easily constructed in other model strains, such as *E. coli*, *Bacillus subtilis*, and *Yeast*, for broad application in enzyme and protein production in the biomanufacturing area. Moreover, the PsiR expression should be further optimized to fit the host requirement.

Traditionally, allulose production has relied on the enzymatic epimerization of fructose by D-allulose-3-epimerase (DAE)[61]. This reaction suffered from reaction equilibrium, resulting low conversion yield of 30%. When glucose served as feedstock, the glucose-to-allulose conversion yield through coupling DAE and glucose isomerase was lower than 18%[62]. Therefore, a complex separation process and vast equipment investment were required to obtain pure allulose. To overcome this bottleneck, we constructed a thermodynamically favorable biosynthetic pathway based on phosphorylation–dephosphorylation steps in *C. glutamicum*. Through systematic metabolic engineering, we enhanced glucose uptake and utilization, while attenuating competing pathways to direct carbon flux toward allulose synthesis. Additionally, the developed allulose-mediated ATCi approach was implemented to dynamically repress *zwf* expression, fine-tuning the flux through the pentose phosphate pathway. This allowed early biomass accumulation while favoring allulose production during later stages, increasing the allulose titer by 68% relative to that without dynamic regulation. As a result, we achieved a glucose-to-allulose conversion yield exceeding 0.43 g/g (Fig. 7f), significantly higher than traditional enzymatic biotransformation method (0.18 g/g). On the basis of this achievement, in future, more genes could be regulated and optimized to further increase the conversion yield and titer. In addition, to achieve dynamic regulation at certain times or cell densities over the course of fermentation, other mutants in the PAB box could be constructed and optimized in ATCi. Beyond microbial synthesis of allulose, such ATCi tool can be extended to reprogram metabolic fluxes for the efficient biosynthesis of other valuable compounds such as N-acetylglucosamine[63], human milk oligosaccharides[64], mannosyl-oligosaccharides[65] in *C. glutamicum*. Overall, this work expands the TF toolbox for protein expression and presents versatile tool for programmable, allulose-triggered metabolic dynamic regulation in synthetic biology and metabolic engineering areas.

Methods

Materials and strains

The chemicals including allulose, glucose, and isopropyl-β-D-1-thiogalactopyranoside (IPTG), were purchased from Sigma-Aldrich (St.Louis, MO, USA). Kanamycin and chloramphenicol for strain selection and growth were obtained from Solarbio (Beijing, China). Strains and plasmids used in this study are listed in Supplementary Tables 6, 7. The primers and gene sequences were shown in Supplementary Data 1. The *E. coli* DH5α (Invitrogen Life Technologies, U.S.A.) strain was used as a cloning host for plasmid construction. The recombinant *E. coli* strains were cultivated in Luria-Bertani (LB) broth at 37 °C with constant shaking at 200 rpm. The *C. glutamicum* ATCC13032 strain served as the host for constructing biosensor library, enzyme expression, and metabolic engineering for allulose synthesis. The *C. glutamicum* ATCC 13032 and its derivatives were cultivated in brain heart infusion (BHI) medium or CGXII minimal medium[66]. Where appropriate, a final concentration of 50 μg/mL kanamycin and 10 μg/mL chloramphenicol was added to culture medium.

Construction of biosensor in *C. glutamicum*

The plasmid pEC-XK99E served as the template to construct the allulose-responsive biosensor in *C. glutamicum*. Firstly, we replaced the LacI operon in pEC-XK99E with H36-PsiR operon, in which the expression of PsiR was controlled by the constitutive promoter of P_{H36}, resulting in a recombinant plasmid pEC-H36-PsiR. Two widely used P_{tuf} and P_{tacM} promoters were further introduced into pEC-H36-PsiR, and the PsiR binding site PsiO sequence (ATTGCA-CAATCGATGGTGCAA) was inserted into different positions, namely the upstream of the −35 box, between the −35 and −10 box, and between the −10 box and RBS, of P_{tuf} and P_{tacM}. The eGFP gene was then constructed at the downstream of the hybrid promoters. The obtained plasmids were transferred into *C. glutamicum* 13032, which resulted in six biosensors, named as PAB1-6. Secondly, we optimized the promoters of PsiR in pEC-PAB6 by replacing P_{H36} with low-strength promoters of P_{L26} and P_{L8O}, medium-strength promoters of P_{sod}, P_{MS}, P_{M6}, and P_{M1O}, high-strength promoters of P_{11F}, P_{tuf}, P_{H9}, and P_{HS}, resulting in the PAB7-PAB16. Thirdly, we optimized the RBS sequence between eGFP and the PsiO operator by using eleven other RBS sequences (Supplementary Data 2), resulting in the PAB17-27. Ultimately, the spacer sequence (TACTT) of P_{M1O} of PsiR in pEC-PAB27 was replaced with five random nucleotides (NNNNN). A variant library was constructed and transferred into *C. glutamicum* 13032. After high-throughput screening of 1400 strains by measuring the fluorescence change under the induction concentration of 50 mM allulose, 78 strains with enhanced fluorescence output relative to PAB27 were obtained.

To measure the green fluorescent of recombinant *C. glutamicum* strains, the cells were first cultivated in 1 mL BHI medium with 25 μg/mL kanamycin in a 24-well plate at 700 rpm and 30 °C overnight. Then, the cells as the seed cultures were transferred into 1 mL of CGXII medium with 10 g/L glucose and 0–200 mM allulose in a 48-well plate to an initial OD_{600} of 0.5. After further cultivation for 12 h, the cells were diluted 10 times in sterile PBS buffer for the fluorescence analysis. The fluorescence intensities of eGFP (excitation, 488 nm; emission 528 nm) and mRFP1 (excitation, 575 nm; emission 610 nm) were determined using a microplate reader (Biotek, Synergy Neo2)[67].

Construction and characterization of PsiR mutants

Site-directed mutations were conducted using PCR methods. The primers used for mutations were listed in Supplementary Data 3. Recombinant plasmid pEC-PAB30 served as the template. The PCR products were digested with DpnI at 37 °C for 2 h and followed by transformation into *E. coli* DH5α cells for plasmid construction. And then, the desired mutations were confirmed by PCR sequencing. To conduct the combinatorial mutation of PsiR, the pEC-PAB30-M1, pEC-PAB30-M2, and pEC-PAB30-M3 served as the template to integrate other beneficial mutations. The obtained plasmids containing genes of PsiR mutants were then transformed into *C. glutamicum* by electroporation. To measure the influence of PsiR mutations on green fluorescence, 0–20 mM allulose was added into the medium to induce eGFP expression. We also measured the green fluorescence values of our designed system PAB30 and PAB30-M4 to 12 sugars, such as seven ketoses like D-allulose, D-fructose, D-sorbose, L-fructose, D-tagatose, D-ribulose, D-xylulose, four aldoses of D-allose, L-rhamnose, L-arabinose, D-xylose, and one sugar alcohol (D-allitol), at the substrate concentration of 20 mM in CGXII buffer.

Strain construction

To construct strain CgM4-MI, we replaced the *eGFP* gene with *ThMI* in pEC-PAB31-M4, and introduced the generated plasmid into *C. glutamicum* 13032. To obtain the strain AutoCgM4-MI, we initially constructed the genes of *alsE* and *yniC* from *E. coli* under the control of strong promoters P_{H36} and P_{tuf} into pXMJ19, resulting in the recombinant plasmid pXM-AlsE-YniC. Then, the pXM-AlsE-YniC and pEC-PAB31-M4-ThMI were introduced together into strain *C. glutamicum* 13032 to generate AutoCgM4-MI.

To construct strain CgdC-M2, the *eGFP* gene in pEC-PAB31-M2 was replaced with *dCpf1* gene[68]. Then, the whole expression cassette containing P_{tacMD}-*dCpf1* and P_{M10}-*PsiR-M2* was cloned and inserted into the plasmid of pK18-Cgl2297, which comprised the upstream and downstream regions (~1 kb) of gene *Cgl2297* in *C. glutamicum* chromosome. The resulting plasmid pK18-Cgl2297-dCpf1-PsiR-M2 was further introduced into *C. glutamicum* 13032 and integrated the *PsiR-dCpf1* expression cassette into the *Cgl2297* site with the aid of homologous recombination method[69], resulting in the strain CgdC-M2. Furthermore, we constructed the gene-integrating vector plasmids pK18-Cgl0331-eGFP and pK18-Cgl2911-mRFP1, and integrated the *eGFP* and *mRFP1* genes into the *Cgl0331* and *Cgl2911* sites, respectively, resulting in strain CgdC-M2-GR.

To repress the gene expression of *eGFP* and *mRFP1* in strain CgdC-M2-GR, we first constructed a *ccdB*-containing template plasmid by inserting the *ccdB* gene under the control of the P_{11F} promoter into the pXMJ19[66]. Based on this template, a series of crRNA expression plasmids, pXMJ19-crRNA-eGFP218, pXMJ19-crRNA-eGFP663, pXMJ19-crRNA-mRFP169, pXMJ19-crRNA-mRFP359, and pXMJ19-crRNA-eGFP218-mRFP169, were generated using the Golden Gate assembly method[70] with crRNAs targeting *eGFP* and *mRFP1*. These plasmids were transformed into strain CgdC-M2-GR, respectively, resulting in strains of CgdC-M2-GR (pXMJ19-crRNA-eGFP218), CgdC-M2-GR (pXMJ19-crRNA-eGFP663), CgdC-M2-GR (pXMJ19-crRNA-mRFP169), CgdC-M2-GR (pXMJ19-crRNA-mRFP359), CgdC-M2-GR (pXMJ19-crRNA-eGFP218-mRFP169).

To develop the allulose synthetic cells, we initially constructed the plasmid pEC-AlsE-YniC by introducing the *alsE* and *yniC* genes into pEC-XK99E, and transformed pEC-AlsE-YniC into strain *C. glutamicum* 13032, resulting in strain CgAll1. To obtain the strain CgAll2, we conducted several genetic modifications in *C. glutamicum* 13032 as follows: i) we constructed the plasmid of pK18- *pfkA* for gene knockout of *pfkA* in *C. glutamicum*; ii) we constructed the plasmid of pK18-O6-iolT1 for replacement of the native operator sequence (GATTGACGGGACATAT) of gene *iolT1* with the mutant sequence (GATTGACGGGGGATAT); iii) we constructed the plasmid of pK18-Cgl2911-BsGlcK-BsPgi for integrating the genes of *glcK* and *pgi* from *Bacillus subtilis* into the *Cgl2911* site, respectively; iv) we sequentially transformed those plasmids into *C. glutamicum* 13032, and obtained the strain CgPIG; v) we introduced the plasmid of pEC-AlsE-YniC into strain CgPIG and obtained strain CgAll2. To construct the strain CgAll3, we transformed the pK18-Cgl2297-dCpf1-PsiR-M2 into strain CgPIG and integrated the *PsiR-dCpf1* expression cassette into the *Cgl2297* site in CgPIG, resulting in strain CgPIG-dC-M2. We also constructed the plasmid of pK18-Cgl2303-crRNA-zwf for integrating the crRNA target to *zwf* into the *Cgl2303* site in CgPIG-dC-M2, resulting in strain CgPIG-dC-M2-zwf. And then, the plasmid pEC-AlsE-YniC was together introduced into strain CgPIG-dC-M2-zwf to obtain CgAll3.

Cell cultivation for enzyme expression

The strain CgM4-MI was cultured in CGXII buffer at 30 °C with an initial glucose concentration of 10 g/L. When the cell density OD_{600} reached 0.6–1.0, 5 mM allulose was added into the medium to induce MI expression. After 24 h of fermentation, the cells were collected and resuspended with Tris-HCl buffer (50 mM, pH 8.0). Then, the cells were lysed by ultrasonic treatment at 4 °C, and centrifuged at 17,000 × *g* for 45 min. The crude enzyme activity of MI was measured in the reaction medium (1 mL), which contained 500 mM fructose, 5 mM Mg^{2+}, Tris-HCl buffer (50 mM, pH 8.0), and 5–150 µL of crude enzyme. The reactions were conducted at 65 °C for 10 min. The samples were then heated at boiling temperature for 10 min and then centrifuged at 17,000 × *g* for 30 min for HPLC analysis. One unit of enzyme activity was defined as the enzyme amount (mL) catalyzing the formation of 1 µmol mannose per min. For the MI expression in strain AutoCgM4-MI, the strain CgM4-MI was cultured in CGXII buffer with 10 g/L glucose at 30 °C for 24 h. And then, the cells were collected for crude enzyme activity analysis.

Cell cultivation for gene regulation and allulose synthesis

To perform the gene repression of eGFP and mRFP1, the cells were initially cultivated in 1 mL BHI medium, and then transferred into CGXII medium containing 5 mM allulose with 0.5% inoculum in 48-well plates. The green and red fluorescence of recombinant strains were measured at different culture times. The CGXII medium without allulose was also used as the control. To perform the allulose synthesis from glucose, the cells of CgAll1, CgAll2, and CgAll3 were cultured in BHI medium, and then transferred into a 250 mL flask containing 20 mL fermentation medium. This medium comprised of 40 g/L corn steep liquor, 20 g/L $(NH_4)_2SO_4$, 50 g/L glucose, 2 g/L urea, 2 g/L KH_2PO_4, 2 g/L K_2HPO_4, 10 mg/L $CaCl_2{\cdot}2H_2O$, 10 mg/L $FeSO_4{\cdot}7H_2O$, 10 mg/L $MnSO_4{\cdot}7H_2O$, 0.1 g/L $MgSO_4{\cdot}7H_2O$. The cultivation was performed at 250 rpm, 30 °C for 24–72 h. When necessary, 10 mg/L chloramphenicol and 25 mg/L kanamycin were supplemented into the culture medium.

Statistics and reproducibility

For all quantitative experiments, data are presented as mean ± SD unless otherwise stated. For bar and line plots, *n* refers to the number of independent biological experiments, which were typically $n = 3$ unless otherwise specified, and are indicated in the figure legends. The statistical tests used (two-sided *t* test with Welch's correction, and one-way ANOVA followed by Dunnett's post hoc test) are specified in the corresponding figure legends together with exact *P* values.

Reporting summary

Further information on research design is available in the Nature Portfolio Reporting Summary linked to this article.

Data availability

All data supporting the findings of this work are available within the article, the Supplementary Information files and the Source Data file. The primers and sequences used in this study are provided in Supplementary Data 1. Details of the molecular dynamic simulation assemblies are provided in Supplementary Data 2. The atomic coordinates of the PsiR-allulose complex have been deposited in the Protein Data Bank under accession code 9KPR. Previously published crystal structures used for comparative analyses are available in the Protein Data Bank under accession codes 2P9H, 4RK1, 7CDX and 3O75. The source data underlying the figures and tables are provided in the Source Data file. Source data are provided with this paper.

References

1. Weidemüller, P., Kholmatov, M., Petsalaki, E. & Zaugg, J. B. Transcription factors: bridge between cell signaling and gene regulation. *Proteomics* **21**, e2000034 (2021).
2. Cheng, F., Tang, X. L. & Kardashliev, T. Transcription factor-based biosensors in high-throughput screening: advances and applications. *Biotechnol. J.* **13**, e1700648 (2018).
3. Rogers, J. K. & Church, G. M. Genetically encoded sensors enable real-time observation of metabolite production. *Proc. Natl. Acad. Sci. USA* **113**, 2388–2393 (2016).
4. Zhang, F., Carothers, J. M. & Keasling, J. D. Design of a dynamic sensor-regulator system for production of chemicals and fuels derived from fatty acids. *Nat. Biotechnol.* **30**, 354–359 (2012).
5. Zhang, Y. et al. Biosensor for branched-chain amino acid metabolism in yeast and applications in isobutanol and isopentanol production. *Nat. Commun.* **13**, 1–14 (2022).
6. Pham, C., Stogios, P. J., Savchenko, A. & Mahadevan, R. Advances in engineering and optimization of transcription factor-based

biosensors for plug-and-play small molecule detection. *Curr. Opin. Biotechnol.* **76**, 102753 (2022).
7. Lu, M. et al. Transcription factor-based biosensor: a molecular-guided approach for advanced biofuel synthesis. *Biotechnol. Adv.* **72**, 108339 (2024).
8. Gao, J. S. et al. Design of a genetically encoded biosensor to establish a high-throughput screening platform for L-cysteine overproduction. *Metab. Eng.* **73**, 144–157 (2022).
9. Gong, X. Y. et al. Engineering of a TrpR-based biosensor for altered dynamic range and ligand preference. *ACS Synth. Biol.* **11**, 2175–2183 (2022).
10. Chen, Y. et al. Tuning the dynamic range of bacterial promoters regulated by ligand-inducible transcription factors. *Nat. Commun.* **9**, 64 (2018).
11. D'Ambrosio, V. et al. Directed evolution of VanR biosensor specificity in Yeast. *Biotechnol. Notes.* **1**, 9–15 (2020).
12. Li, J. et al. Engineering transcription factor xylS for sensing phthalic acid and terephthalic acid: an application for enzyme evolution. *ACS Synth. Biol.* **11**, 1106–1113 (2022).
13. Wu, T. et al. Engineering transcription factor BmoR mutants for constructing multifunctional alcohol biosensors. *ACS Synth. Biol.* **11**, 1251–1260 (2022).
14. Swint-Kruse, L. & Matthews, K. S. Allostery in the LacI/GalR family: variations on a theme. *Curr. Opin. Microbiol.* **12**, 129–137 (2009).
15. Tack, D. S. et al. The genotype-phenotype landscape of an allosteric protein. *Mol. Syst. Biol.* **17**, e10179 (2021).
16. Yuan, Y., Deng, J. & Cui, Q. Molecular dynamics simulations establish the molecular basis for the broad allostery hotspot distributions in the tetracycline repressor. *J. Am. Chem. Soc.* **144**, 10870–10887 (2022).
17. Suckow, J. et al. Genetic studies of the Lac repressor. XV: 4000 single amino acid substitutions and analysis of the resulting phenotypes on the basis of the protein structure. *J. Mol. Biol.* **260**, 509–523 (1996).
18. Fu, G. et al. An operator-based expression toolkit for *Bacillus subtilis* enables fine-tuning of gene expression and biosynthetic pathway regulation. *Proc. Natl. Acad. Sci. USA.* **119**, e2119980119 (2022).
19. Rosano, G. L. & Ceccarelli, E. A. Recombinant protein expression in *Escherichia coli*: advances and challenges. *Front. Microbiol.* **5**, 172 (2014).
20. Li, Y. et al. A cross-species inducible system for enhanced protein expression and multiplexed metabolic pathway fine-tuning in bacteria. *Nucleic Acids Res.* **53**, gkae1315 (2025).
21. Lewis, M. et al. Crystal structure of the lactose operon repressor and its complexes with DNA and inducer. *Science.* **271**, 1247–1254 (1996).
22. Jacob, F. & Monod, J. Genetic regulatory mechanisms in the synthesis of proteins. *J. Mole. Biol.* **3**, 318–356 (1961).
23. Li, Z., Kessler, W., van den, Heuvel, J. & Rinas, U. Simple defined autoinduction medium for high-level recombinant protein production using T7-based *Escherichia coli* expression systems. *Appl. Microbiol. Biotechnol.* **91**, 1203–1213 (2011).
24. Landberg, J., Mundhada, H. & Nielsen, A. T. An autoinducible trp-T7 expression system for production of proteins and biochemicals in *Escherichia coli*. *Biotechnol. Bioeng.* **117**, 1513–1524 (2020).
25. Liu, M. et al. OptoLacI: optogenetically engineered lactose operon repressor LacI responsive to light instead of IPTG. *Nucleic Acids Res.* **52**, 8003–8016 (2024).
26. Zhang, Y. et al. Development and application of an arabinose-inducible expression system by facilitating inducer uptake in *Corynebacterium glutamicum*. *Appl. Environ. Microbiol.* **78**, 5831–5838 (2012).
27. Tang, R.-Q. et al. Design, evolution, and characterization of a xylose biosensor in *Escherichia coli* using the XylR/xylO system with an expanded operating range. *ACS Synth. Biol.* **9**, 2714–2722 (2020).
28. Yue, J., Fu, G., Zhang, D. & Wen, J. A new maltose-inducible high-performance heterologous expression system in *Bacillus subtilis*. *Biotechnol. Lett.* **39**, 1237–1244 (2017).
29. Armetta, J. et al. Biosensor-based enzyme engineering approach applied to psicose biosynthesis. *Synth. Biol.* **4**, 1–10 (2019).
30. Xu, B. et al. Directed evolution of *Escherichia coli* Nissle 1917 to utilize allulose as sole carbon source. *Small Methods*. **8**, 2301385 (2024)
31. Xie, X., Li, C., Ban, X., Yang, H., & Li, Z. D-allulose 3-epimerase for low-calorie D-allulose synthesis: microbial production, characterization, and applications. *Crit. Rev. Biotechnol.* **45**, 353–372 (2024)
32. Li, C. et al. Growth-coupled evolutionary pressure improving epimerases for D-allulose biosynthesis using a biosensor-assisted in vivo selection platform. *Adv. Sci.* **11**, 2306478 (2024).
33. Du, Y. et al. Construction of an ultra-strong P_{tacM} promoter via engineering the core-element spacer and 5′untranslated region for versatile applications in *Corynebacterium glutamicum*. *Biotechnol. Notes.* **3**, 88–96 (2022).
34. Yim, S. S., An, S. J., Kang, M., Lee, J. & Jeong, K. J. Isolation of fully synthetic promoters for high-level gene expression in *Corynebacterium glutamicum*. *Biotechnol. Bioeng.* **110**, 2959–2969 (2013).
35. Abramson, J. et al. Accurate structure prediction of biomolecular interactions with AlphaFold 3. *Nature* **630**, 493–500 (2024).
36. Liao, Q. et al. Long time-scale atomistic simulations of the structure and dynamics of transcription factor-DNA recognition. *J. Phys. Chem. B.* **123**, 3576–3590 (2019).
37. Xu, J., Liu, S., Chen, M., Ma, J. & Matthews, K. S. Altering residues N125 and D149 impacts sugar effector binding and allosteric parameters in *Escherichia coli* lactose repressor. *Biochemistry* **50**, 9002–9013 (2011).
38. Fu, Y. et al. Structural and functional analyses of the cellulase transcription regulator CelR. *FEBS Lett* **592**, 2776–2785 (2018).
39. Chovancova, E. et al. CAVER 3.0: a tool for the analysis of transport pathways in dynamic protein structures. *PLoS Comput. Biol.* **8**, e1002708 (2012).
40. Fu, H., Shao, X., Cai, W. & Chipot, C. Taming rugged free energy landscapes using an average force. *Acc. Chem. Res.* **52**, 3254–3264 (2019).
41. Zong, Z. et al. Elucidation of the noncovalent interactions driving enzyme activity guides branching enzyme engineering for α-glucan modification. *Nat. Commun.* **15**, 8760 (2024).
42. Zhou, J. et al. Structural basis for the acylation reaction of alpha-coronavirus 3C-like protease. *ACS Catal.* **14**, 8330–8342 (2024).
43. Yu, H. & Dalby, P. A. Coupled molecular dynamics mediate long-and short-range epistasis between mutations that affect stability and aggregation kinetics. *Proc. Natl. Acad. Sci. USA.* **115**, 1810324115 (2018).
44. Glasgow, A. et al. Ligand-specific changes in conformational flexibility mediate long-range allostery in the *lac* repressor. *Nat. Commun.* **14**, 1179 (2023).
45. Lu, C. et al. Site-resolved energetic information from HX–MS experiments. *Nat. Chem. Biol.* https://doi.org/10.1038/s41589-025-02049-1 (2025).
46. Wells, M. L. et al. Conserved energetic changes drive function in an ancient protein fold. bioRxiv https://doi.org/10.1101/2025.04.02.646877 (2025).
47. Hellman, L. & Fried, M. Electrophoretic mobility shift assay (EMSA) for detecting protein–nucleic acid interactions. *Nat. Protoc.* **2**, 1849–1861 (2007).
48. Jerabek-Willemsen, M. et al. Microscale thermophoresis: interaction analysis and beyond. *J. Mol. Struct.* **1077**, 101–113 (2014).
49. Jin, P. et al. Efficient bioconversion of high-concentration D-fructose into D-mannose by a novel N-acyl-D-glucosamine 2-epimerase

from *Thermobifida halotolerans*. *Catal. Sci. Technol.* **11**, 1922–1930 (2021).
50. Cui, W. et al. Creation of an orthogonal and universal auto-inducible gene expression platform by reprogramming a two-component signal circuit for efficient production of industrial enzymes. *Int. J. Biol. Macromol.* **283**, 137781 (2024).
51. Brüsseler, C. et al. The myo-inositol/proton symporter IolT1 contributes to D-xylose uptake in *Corynebacterium glutamicum*. *Bioresource Technol.* **249**, 953–961 (2017).
52. Liu, Y. et al. Microbial synthesis of sedoheptulose from glucose by metabolically engineered *Corynebacterium glutamicum*. *Microb. Cell Fact.* **23**, 251 (2024).
53. Yang, J. et al. De novo artificial synthesis of hexoses from carbon dioxide. *Sci. Bull.* **68**, 2370–2381 (2023).
54. Liu, J., Zhang, W. & Rao, Z. Transcriptional regulator-based biosensors for biomanufacturing in *Corynebacterium glutamicum*. *Microbiol. Res.* **297**, 128169 (2025).
55. Liu, Z. et al. Optimization of ultrahigh-throughput screening assay for protein engineering of D-allulose 3-epimerase. *Biomolecules*. **12**, 1547 (2022).
56. Chen, B. et al. Biosensor-assisted evolution of RhaD for enhancing the biosynthetic yield of D-allulose. *Food Biosci.* **60**, 104426 (2024).
57. Yao, Z. et al. Unlocking green biomanufacturing potential: superior heterologous gene expression with a T7 integration overexpression system in *Bacillus subtilis*. *ACS. Synth. Biol.* **14**, 1977–1987 (2024).
58. Wilms, B. et al. High-cell-density fermentation for production of L-*N*-carbamoylase using an expression system based on the *Escherichia coli* rhaBAD promoter. *Biotechnol. Bioeng.* **73**, 95–103 (2001).
59. Tan, S. Z. & Prather, K. L. Dynamic pathway regulation: recent advances and methods of construction. *Curr. Opin. Chem. Biol.* **41**, 28–35 (2017).
60. Hauk, P. et al. Homologous quorum sensing regulatory circuit: a dual-input genetic controller for modulating quorum sensing-mediated protein expression in *E. coli*. *ACS Synth Biol.* **9**, 2692–2702 (2020).
61. Zhang, W. et al. D-allulose, a versatile rare sugar: recent biotechnological advances and challenges. *Crit. Rev. Food Sci. Nutr.* **63**, 5661–5679 (2023).
62. Men, Y. et al. Co-expression of D-glucose isomerase and D-psicose 3-epimerase: development of an efficient one-step production of D-psicose. *Enzyme Microb. Technol.* **64**, 1–5 (2014).
63. Li, Z. et al. Engineering *Corynebacterium glutamicum* for the efficient production of N-acetylglucosamine. *Bioresour. Technol.* **390**, 129865 (2023).
64. Lee, Y.-G. et al. De novo biosynthesis of 2′-fucosyllactose by bioengineered *Corynebacterium glutamicum*. *Biotechnol. J.* **19**, 2300461 (2024).
65. Tian, C. et al. Artificially designed routes for the conversion of starch to value-added mannosyl compounds through coupling in vitro and in vivo metabolic engineering strategies. *Metab. Eng.* **61**, 215–224 (2020).
66. Yang, J. et al. Biosynthesis of rare ketoses through constructing a recombination pathway in an engineered *Corynebacterium glutamicum*. *Biotechnol. Bioeng.* **112**, 168–180 (2015).
67. Wu, Y. et al. CAMERS-B: CRISPR/Cpf1 assisted multiple-genes editing and regulation system for *Bacillus subtilis*. *Biotechnol. Bioeng.* **117**, 1817–1825 (2020).
68. Li, M. et al. Efficient multiplex gene repression by CRISPR-dCpf1 in *Corynebacterium glutamicum*. *Front. Bioeng. Biotechnol.* **8**, 357 (2020).
69. Yang, J. et al. Development of food-grade expression system for D-allulose 3-epimerase preparation with tandem isoenzyme genes in *Corynebacterium glutamicum* and its application in conversion of cane molasses to D-allulose. *Biotechnol. Bioeng.* **116**, 745–756 (2019).
70. Engler, C. & Marillonnet, S. Golden Gate cloning. *Methods Mol. Biol.* **1116**, 119–131 (2014).

Acknowledgements

This work was supported by the National Natural Science Foundation of China (32271545 [J.Y.], 32572514 [J.Y.]), Natural Science Foundation Program of Tianjin Grant Type A (25JCJQJC00130 [J.Y.]), Major Program of Haihe Laboratory of Synthetic Biology (22HHSWSS00016 [J.Y.] and 22HHSWSS00003 [J.Y.]), Tianjin Major Science and Technology Projects and Engineering Programs (National Key Laboratory Projects) (25ZXZSSS00010 [P.C.]), Youth Promotion Association of Chinese Academy of Sciences (2021176 [J.Y.]), We thank the staffs from beamlines of BL02U1 (BL17U)/BL17UM/BL18U1 in National Facility for Protein Science in Shanghai (NFPS) at Shanghai Synchrotron Radiation Facility (SSRF) for assistance during data collection.

Author contributions

Q.D. performed rational design and engineering of PsiR, constructed the ATCi system, and prepared the article draft. P.C. constructed the AMAE system. Z.G. engineered LacI and characterized its variants. H.W. and W.L. solved the crystal structure of PsiR-allulose complex. Y.Z. analyzed the fluorescence data and measured the enzyme activity. J.Z. performed the gene knockout and chromosomal integration in *C. glutamicum*. Y.M. performed the microbial fermentation for allulose synthesis. Y.S., and J.Y. designed the experiments and revised the manuscript.

Competing interests

The authors declare no competing interests.

Additional information

Supplementary information The online version contains supplementary material available at https://doi.org/10.1038/s41467-025-67669-6.

Correspondence and requests for materials should be addressed to Yuanxia Sun or Jiangang Yang.

Peer review information *Nature Communications* thanks Shihui Yang and the other anonymous reviewers for their contribution to the peer review of this work. A peer review file is available.